How clustered protocadherin binding specificity is tuned for neuronal self/non-self-recognition

Kerry M. Goodman[1,7], Phinikoula S. Katsamba[1,7], Rotem Rubinstein[5,6]

Göran Ahlsén[1], Fabiana Bahna[1], Seetha Mannepalli[1], Hanbin Dan[4],

Rosemary Sampogna[4], Lawrence Shapiro[1,2*], and Barry Honig[1,2,3,4*]

[1]Zuckerman Mind, Brain and Behavior Institute, Columbia University, New York, NY 10027, USA
[2]Department of Biochemistry and Molecular Biophysics, Columbia University, New York, NY 10032, USA
[3]Department of Systems Biology, Columbia University, New York, NY 10032, USA
[4]Department of Medicine, Division of Nephrology, Columbia University, New York, NY 10032, USA
[5]School of Neurobiology, Biochemistry and Biophysics, Tel Aviv University, Israel
[6]Sagol School of Neuroscience, Tel Aviv University, Israel
[7]Equal contribution
[*]Correspondence: lss8@columbia.edu (L.S.); bh6@cumc.columbia.edu (B.H.)

1 **Abstract (152 words)**

2 The stochastic expression of fewer than 60 clustered protocadherin (cPcdh) isoforms provides

3 diverse identities to individual vertebrate neurons and a molecular basis for self/non-self-

4 discrimination. cPcdhs form chains mediated by alternating *cis* and *trans* interactions between

5 apposed membranes, which has been suggested to signal self-recognition. Such a mechanism

6 requires that cPcdh *cis* dimers form promiscuously to generate diverse recognition units, and that

7 *trans* interactions have precise specificity so that isoform mismatches terminate chain growth.

8 However, the extent to which cPcdh interactions fulfill these requirements has not been

9 definitively demonstrated. Here we report biophysical experiments showing that cPcdh *cis*

10 interactions are promiscuous, but with preferences favoring formation of heterologous *cis* dimers.

11 *Trans*-homophilic interactions are remarkably precise, with no evidence for heterophilic

12 interactions between different isoforms. A new C-type cPcdh crystal structure and mutagenesis

13 data help to explain these observations. Overall, the interaction characteristics we report for cPcdhs

14 help explain their function in neuronal self/non-self-discrimination.

Introduction

Clustered protocadherins (cPcdhs) are a large family of cadherin-like proteins named for the clustered arrangement of their genes in vertebrate genomes (Wu and Maniatis, 1999; Wu et al., 2001). cPcdhs play roles in many facets of neural development (Peek et al., 2017), including circuit development, most notably neurite self-avoidance in vertebrates (Kostadinov and Sanes, 2015; Lefebvre et al., 2012; Mountoufaris et al., 2017), and tiling (Chen et al., 2017). In self-avoidance, neurites from the same neuron (sister neurites) actively avoid one another, whereas neurons from different neurons can freely interact. Tiling is similar to self-avoidance, but in tiling all neurons acquire the same identity, so that there is uniform repulsion among self- and non-self neurites (Chen et al., 2017). Self-avoidance among sister neurites leads to the characteristic arbor structures of dendritic trees, and prevents the formation of self-synapses (Kostadinov and Sanes, 2015; Lefebvre et al., 2012).

The molecular mechanisms through which neurons discriminate self from non-self, differ between vertebrate and most invertebrate animals. For arthropod invertebrates such as *Drosophila melanogaster*, self-avoidance is mediated by immunoglobulin superfamily Dscam1 cell surface proteins. The stochastic alternative splicing of *Dscam1* pre-mRNAs can, in principle, generate 19,008 distinct extracellular isoforms; the vast majority of which, based on ELISA-based binding assay, mediate homophilic recognition (Miura et al., 2013; Schmucker et al., 2000; Wojtowicz et al., 2004; Wojtowicz et al., 2007). Each neuron expresses a repertoire estimated at 10–50 isoforms and the large number of Dscam1 isoforms ensures a low probability that any two contacting neurons will have an identical or even a similar isoform repertoire thus minimizing the chance of inappropriate avoidance between non-self neurons (Hattori et al., 2009).

In mammalian nervous systems cPcdh isoform expression is controlled by the unique organization of three tandem gene clusters, *Pcdhα*, *Pcdhβ*, and *Pcdhγ* (Wu and Maniatis, 1999), with each cluster containing multiple variable exons, which encode full cPcdh ectodomain regions with six extracellular cadherin (EC) domains, a single transmembrane region, and a short cytoplasmic extension (Figure 1A). The *Pcdhα* and *Pcdhγ* gene clusters also contain three 'constant' exons that encode cluster-specific intracellular domains. The last two variable exons in the *Pcdhα* gene

45 cluster and the last three variable exons of the *Pcdhγ* gene cluster diverge in sequence from other

46 cPcdh isoforms and are referred to as 'C-type' cPcdhs (Wu and Maniatis, 1999; Wu et al., 2001).

47 Sequence differences further subdivide *Pcdhγ* genes into two subfamilies – *Pcdhγ*A and *Pcdhγ*B

48 (Wu and Maniatis, 1999). The full mouse cPcdh complement is comprised of 53 non-C-type

49 cPcdhs, commonly known as alternate cPcdhs (α1–12, β1–22, γA1–12, and γB1–7), whose

50 expression choices vary stochastically between cells through alternate promoter choice (Canzio

51 and Maniatis, 2019); and 5 C-type cPcdhs (αC1, αC2, γC3, γC4, and γC5), which are constitutively

52 expressed. cPcdh expression, either stochastic or constitutive, varies between cell types: For

53 example, olfactory sensory neurons express ~5–10 cPcdhs stochastically; Purkinje neurons express

54 ~10 alternate cPcdhs stochastically and all five C-types constitutively (Esumi et al., 2005; Kaneko

55 et al., 2006); and serotonergic neurons express just αC2 constitutively (Canzio and Maniatis, 2019;

56 Chen et al., 2017). While the cPcdh and Dscam1 systems bear striking similarities, the relatively

57 small number of cPcdh isoforms – fewer than 60 – has presented a significant challenge to

58 generation of sufficient diversity to provide mammalian neurons with functionally unique

59 identities.

60

61 Solution biophysics and functional mutagenesis studies, have shown that cPcdhs interact in *trans*

62 through antiparallel interactions between their EC1–EC4 regions (Rubinstein et al. 2015), and

63 crystal structures of alternate α, β, and γ cPcdh *trans*-homodimers have revealed interfaces

64 involving EC1 interacting with EC4 and EC2 with EC3 (Figure 1B) (Goodman et al., 2016a;

65 Goodman et al., 2016b; Nicoludis et al., 2016; Rubinstein et al., 2015; Thu et al., 2014). cPcdhs

66 also form *cis* dimers through their membrane-proximal EC5–EC6 regions, and are presented on

67 cell surfaces as *cis* dimers (Goodman et al., 2017; Rubinstein et al., 2015; Thu et al., 2014). Crystal

68 structures of *cis*-interacting protocadherin ectodomains (Brasch et al., 2019; Goodman et al., 2017)

69 have revealed an asymmetrical interaction mode, where one molecule interacts through elements

70 of EC5 and EC6, and the other interacts exclusively through EC6 (Figure 1C). To date, structural

71 studies of C-type cPcdh interactions have not been available. Here we extend our molecular

72 understanding of cPcdhs to C-type isoforms as well, with the goal of understanding the

73 evolutionary design of the entire family.

74

75   In order to explain how about 60 cPcdh isoforms can provide a comparable or even greater level

76   of neuronal diversity as 19,000 Dscam isoforms, Rubinstein et al. (2015) proposed that cPcdhs

77   located on apposed membrane surfaces would form an extended zipper-like lattice through

78   alternating *cis* and *trans* interactions (Figure 1D). In self-interactions – between two membranes

79   with identical cPcdh repertoires – these chains would grow to form large structures, limited mainly

80   by the number of molecules (Brasch et al., 2019; Rubinstein et al., 2015). However, in non-self-

81   interactions – between two membranes with differing cPcdh repertoires – such large linear

82   assemblies would not form since even a single mismatch between expressed isoforms would

83   terminate chain assembly (Brasch et al., 2019; Rubinstein et al., 2017; Rubinstein et al., 2015).

84   This "isoform-mismatch chain-termination model" for the "barcoding" of vertebrate neurons

85   envisions the assembly of long cPcdh chains between sites of neurite-neurite contact to represent

86   the signature of "self", which is then translated by downstream signaling that leads to self-

87   avoidance (Fan et al., 2018). X-ray crystallographic studies and cryo-electron tomography (cryo-

88   ET) studies of the full-length cPcdh ectodomains bound between the surfaces of adherent

89   liposomes revealed the existence of linear zippers thus providing strong evidence supporting the

90   validity of the model (Brasch et al., 2019). However, crucial questions remain unanswered. Here,

91   a number of them are addressed.

92

93   1) For the proposed mechanism to successfully explain neuronal barcoding, *cis* interactions must

94   be promiscuous to generate diverse repertoires of *cis*-dimeric biantennary 'interaction units', while

95   *trans* interactions must be highly specific so that mismatched isoforms do not inappropriately

96   enable growth of the chain through heterophilic interactions. While cell aggregation assays have

97   suggested *trans* homophilic specificity, these assays only reflect a *competition* between different

98   cell populations and thus don't inform as to the strength of heterophilic interactions. Moreover,

99   the results of cell aggregation assays depend critically on the *relative* strengths of homophilic and

100   heterophilic interactions and thus do not inform as to actual binding affinities (Honig and Shapiro,

101   2020). It is thus necessary to establish the extent to which heterophilic *trans* interactions are truly

102   disallowed.

103

104   2) The assumption that *cis* interactions are promiscuous is based in large part on the fact that α-

105   cPcdhs and γC4 cannot reach the cell surface without binding *in cis* to another "carrier" isoform

(Bonn et al., 2007; Goodman et al., 2016b; Murata et al., 2004; Schreiner and Weiner, 2010; Thu et al., 2014). As is the case for *trans* interactions, the strength of *cis* interactions has only been probed quantitatively in a small number of cases so that the term "promiscuous" is qualitative at best. In fact, as compared to γB and β cPcdh isoforms, most γA-Pcdhs do not form measurable *cis* homodimers in solution (Goodman et al., 2016b) (Figure 4—source data 1). Nevertheless, all γA-Pcdhs are still able to reach the cell surface when expressed alone (Thu et al., 2014). This observation can be understood if the *cis* dimerization affinity of γA-Pcdhs is large enough to enable them to dimerize in the 2D membrane environment (Goodman et al., 2016b; Wu et al., 2013). Nevertheless, their weak dimerization affinities suggest, more generally, that cPcdhs may exhibit a range of *cis* dimerization affinities. We establish below that a wide range of affinities does in fact exist and, strikingly, most homophilic *cis* interactions are weaker than their heterophilic counterparts. We consider the functional implications of this novel observation in the discussion.

3) Structures have not yet been determined for complete C-type cPcdh ectodomains. Yet these isoforms play unique functional roles, some of which have no apparent connection to isoform diversity. For example, a single C-type isoform is sufficient for tiling which can be simply understood in terms of the formation of zippers containing identical homodimers so that all interacting neurons will avoid one another (Chen et al., 2017). Moreover, Garrett and coworkers discovered that neuronal survival and postnatal viability is controlled solely by γC4 suggesting a function that is unique to this isoform (although it presumably requires β and/or other γ carriers to reach the cell surface) (Garrett et al., 2019). Additionally, a recent paper by Iqbal and coworkers has shown that genetic γC4 variants cause a neurodevelopmental disorder which is potentially linked to γC4's role in programmed cell death of neuronal cells (Iqbal et al., 2021). Below we report extensive biophysical interaction studies of C-type isoform ectodomains and report the first crystal structure of a *trans* dimer formed by γC4. Our findings reveal that the specialized functions of C-type cPcdhs probably do not involve unique structural or biophysical properties of their ectodomains.

Overall, in accordance with the requirements of the isoform-mismatch chain-termination model, we find that *trans*-homophilic interactions are remarkably precise, with no evidence for heterophilic interactions between different cPcdh isoforms. In contrast cPcdh *cis* interactions are

137 largely promiscuous but with relatively weak intra-subfamily and, especially, homophilic
138 interactions. Possible implications of this somewhat surprising finding are considered in the
139 discussion. Our study reveals how the extraordinary demands posed by the need to assign each
140 neuron with a unique identity are met by an unprecedented level of protein-protein interaction
141 specificity.

142

143 **Results**

144 *cPcdh trans interactions are strictly homophilic*

145 We generated biotinylated ectodomain fragments containing the *trans*-interacting EC1–4 regions
146 (Nicoludis et al., 2015; Rubinstein et al., 2015) of six representative α, β, γA, and γB mouse cPcdh
147 isoforms – α7, β6, β8, γA8, γA9 and γB2 – which include the most closely related isoforms by
148 sequence identity from the β and γA subfamilies (β6/8 and γA8/9) (Rubinstein et al., 2015). These
149 molecules were coupled over independent Neutravidin-immobilized flow cells and *trans*-
150 interacting ectodomain fragments of multiple members of each mouse cPcdh subfamily, including
151 the C-types (α4, α7, α12, β6, β8, γA4, γA8, γA9, γB2, γB4, γB5, αC2, γC3, γC4, and γC5), were
152 then flowed over the six cPcdh surfaces to assess their binding. The surface plasmon resonance
153 (SPR) binding profiles reveal strictly homophilic binding (Figure 2A). All ectodomain fragments
154 used in these SPR experiments were confirmed to form homodimers in solution by sedimentation
155 equilibrium analytical ultracentrifugation (AUC) (Figure 2—source data 1), validating that these
156 proteins are well-behaved and active. Remarkably, no heterophilic binding was observed for any
157 of the analytes over any of the six surfaces (Figure 2A). Even β6/8 and γA8/9 that have 92% and
158 82% sequence identities respectively in their *trans*-binding EC1–4 regions exhibit no heterophilic
159 binding. We estimate that, for heterophilic *trans*-dimers, the lower limit for the dissociation
160 constant (K_D) would be ~200 μM. Mutations designed to disrupt α7, β6, and γA8 *trans* interaction
161 inhibited homophilic binding, demonstrating that the observed binding occurs via the *trans*
162 interface (Figure 2—figure supplement 1A) (Goodman et al., 2016a; Goodman et al., 2016b;
163 Rubinstein et al., 2015). This behavior is unlike that of other adhesion receptor families where,
164 whether they display homophilic or heterophilic preferences, the signal is never as binary as the
165 one shown in Figure 2 (Honig and Shapiro, 2020).

166

167   Much of the original evidence as to homophilic specificity was based on cell aggregation assays

168   (Rubinstein et al., 2015; Schreiner and Weiner, 2010; Thu et al., 2014) and it is of interest to

169   compare the results obtained from these assays to those obtained from SPR. We do this in the

170   context of examining the heterophilic binding specificity between $\beta6_{1-4}$ and $\beta8_{1-4}$ *trans* fragments

171   that share 92% sequence identity and differ at only five residues (Figure 2—figure supplement

172   2A), within their respective binding interfaces (Goodman et al., 2016a). Each of these residues

173   was mutated individually and in combination. Figure 2—figure supplement 2B and C display SPR

174   profiles and cell aggregation images, respectively, for wild type $\beta6$ and $\beta8$ and for the various

175   mutations. We first note that changing all five residues in $\beta6$ to those of $\beta8$ generates a mutant

176   protein with essentially wild type $\beta8$ properties; it binds strongly to $\beta8$ but not to $\beta6$ as seen in

177   SPR and also forms mixed aggregates with $\beta8$ but not $\beta6$. In contrast, most of the single residue

178   mutants retain $\beta6$-like properties in both assays whereas double and triple mutants exhibit

179   intermediate behavior between $\beta6$ and $\beta8$. These results demonstrate that despite the 92% sequence

180   identity between $\beta6$ and $\beta8$, their highly specific homophilic properties can be attributed to five

181   interfacial residues. Moreover, the cell aggregation assays are consistent with the heterophilic

182   binding traces measured by SPR; cells expressing mutants that generate strong SPR signals with

183   either wild type $\beta6$ or $\beta8$ also form mixed aggregates with cells expressing the same wild-type

184   protein.

185

186   Of note, *trans*-interacting fragments of all four C-type cPcdhs tested showed no binding over the

187   alternate cPcdh SPR surfaces (Figure 2A). To test whether C-type cPcdhs also show strict

188   homophilic specificity with respect to each other we coupled biotinylated *trans*-interacting

189   fragments of αC2, γC3, γC4, and γC5 to SPR chips and passed the same four fragments alongside

190   alternate cPcdh *trans* fragments over these four surfaces. Only homophilic binding was observed,

191   with each of the four C-type fragments binding to its cognate partner and no other isoform (Figure

192   2B). Disrupting the γC5 *trans* interaction with the S116R mutation (Rubinstein et al., 2015),

193   inhibited binding to the γC5 surface, demonstrating that the observed binding occurs via the *trans*

194   interface (Figure 2—figure supplement 1B).

195

196   In contrast to the other C-type isoforms, αC1 does not mediate cell-cell interactions in cell

197   aggregation assays even when co-expressed with cPcdhs that facilitate cell-surface delivery of γC4

198   (Thu et al., 2014). Although we have been able to produce an αC1 EC1–4 fragment the

199   recombinant molecule forms disulfide-linked multimers which are likely non-native, precluding

200   confident examination of αC1's potential *trans* interactions. Notably, the sequence of mouse αC1

201   reveals the EC3:EC4 linker does not contain the full complement of calcium-coordinating residues,

202   which may impact the structure and binding properties of this protein (Thu et al., 2014).

203

204   Since all the cPcdh *trans* fragment molecules used in these SPR experiments homodimerize our

205   SPR data cannot be used to determine accurate binding affinities (Rich and Myszka, 2007). We

206   therefore used AUC to measure the *trans*-homodimer K_{DS} (Figure 2—source data 1) revealing a

207   >200-fold range of binding affinities, from 2.9 μM ($α7_{1–5}$) to >500 μM ($γC4_{1–4}$). Regardless of

208   their *trans* binding affinity, all cPcdhs (except αC1) have previously been shown to effectively

209   mediate cell-cell interactions in cell aggregation assays (Schreiner and Weiner, 2010; Thu et al.,

210   2014).

211

212   ***Crystal structure of C-type cPcdh γC4 reveals EC1–4-mediated head-to-tail* trans *dimer interaction***

213   The biophysical properties of C-type cPcdhs pose a number of interesting questions: Despite their

214   more divergent sequences compared with alternate cPcdhs, AUC data has confirmed that C-type

215   cPcdhs αC2, γC3, and γC5 form *trans*-dimers using their EC1–4 domains (Goodman et al., 2016b;

216   Rubinstein et al., 2015). However, $γC4_{1–4}$ behaved as a very weak dimer in AUC (K_D > 500 μM;

217   Figure 2—source data 1), nevertheless full-length γC4 can mediate cell aggregation when

218   delivered to the cell surface by co-expression with a 'carrier' cPcdh (Thu et al., 2014). In addition,

219   C-type isoforms have unique expression profile and function compared to alternate cPcdhs (Canzio

220   and Maniatis, 2019; Mountoufaris et al., 2016). However, there are no published crystal structures

221   of C-type cPcdh *trans* dimers. We therefore sought to crystallize a mouse C-type cPcdh engaged

222   in a *trans* interaction and obtained two distinct crystal forms of $γC4_{EC1–4}$, one at 2.4 Å resolution

223   (crystallized at pH 7.5) and the other with anisotropic diffraction at 4.6/3.9/3.5 Å resolution (Figure

224   3A, Figure 3—figure supplement 1A,B, Figure 3—source data 1) (crystallized at pH 6.0). Both

225   crystal structures revealed an EC1–4-mediated head-to-tail *trans* dimer: The 4.6/3.9/3.5 Å crystal

226   structure appears to have a fully intact *trans* interface with a total buried surface area of 3800 Å^2,

227   which is a similar size to other cPcdh *trans* dimer interfaces (Goodman et al., 2016a; Goodman et

228   al., 2016b; Nicoludis et al., 2016) (Figure 3B, Figure 3—figure supplement 1B). However, the 2.4

229   Å structure had an apparently partially disrupted EC2:EC3 interface resulting in a total buried

230   surface area of just 2900 Å^2 (Figure 3B). The difference between the two structures may be due to

231   differences in the pH of the crystallization and its effect on the ionization state of the three

232   histidines present in the EC2:EC3 interface (Figure 3B). The differences could also reflect distinct

233   states of a dynamic interaction, as has previously been observed crystallographically (Nicoludis et

234   al., 2016; Goodman et al., 2016b) and explored computationally for other cPcdh *trans* interactions

235   (Nicoludis et al., 2019).

236

237   Despite the γC4 *trans* dimer sharing structural similarity and the interface having similar buried

238   surface area as alternate α, β, γA, and γB cPcdhs and δ2 non-clustered Pcdhs (Figure 3—source

239   data 2) (Cooper et al., 2016; Goodman et al., 2016a; Goodman et al., 2016b; Harrison et al., 2020;

240   Hudson et al., 2021; Nicoludis et al., 2016), its binding affinity is very weak. The two most

241   structurally similar molecules to γC4 over their *trans* interacting domains, cPcdh γB2 and non-

242   clustered Pcdh19. γB2 and Pcdh19 have *trans* dimer K$_D$s of 21.8 μM and 0.48 μM respectively

243   (Harrison et al., 2020), while that of γC4 is >500 μM. Comparison between the γB2 and γC4 dimer

244   interfaces highlighted two buried charges in the γC4 *trans* interface, E78 and D290, which could

245   potentially contribute to the low interaction affinity (Figure 3C). To test this, we mutated these

246   two residues to neutral amino acids and used AUC to determine whether the binding affinity

247   increased: The two D290 mutations we tested, D290A and D290N, had no measurable impact on

248   binding; but mutating E78 significantly increased the binding affinity with γC4$_{EC1-4}$ E78A showing

249   a K$_D$ of 58 μM and γC4$_{EC1-4}$ E78Q, 83 μM (Figure 3D, Figure 3—figure supplement 1C). The

250   equivalent residue to E78 in γB2 is also charged (D77) and forms a salt bridge with K340 in the

251   γB2 dimer (Figure 3C). To assess whether generating a similar salt bridge in γC4 would

252   compensate for the negative impact of E78 on dimer affinity we generated an S344R mutant.

253   Similar to the E78 mutants, γC4$_{EC1-4}$ S344R also had a stronger binding affinity than wild type

254   with a K$_D$ of 112 μM (Figure 3D, Figure 3-figure supplement 1C). It appears then that E78 plays

255 an important role in weakening cPcdh γC4's *trans* interaction although the functional reasons for
256 γC4's weak *trans* interaction are unclear.
257
258 ***Clustered protocadherin cis interactions are promiscuous with a range of interaction strengths***
259 To systematically investigate cPcdh *cis* interactions, we coupled *cis*-interacting fragments of
260 mouse β9, γA4, γA9, γB2, αC2, γC3, and γC5 to SPR chip surfaces. *Cis*-interacting fragments of
261 three members from each of the β, γA, and γB subfamilies (β1, β6, β9, γA3, γA4, γA9, γB2, γB5,
262 γB7) alongside αC2, γC3, and γC5 fragments were flowed over the seven surfaces to detect their
263 heterophilic binding (Figure 4A). Alternate α-cPcdhs, and the C-types αC1 and γC4 were not
264 included in this study since EC6-containing fragments of these molecules cannot be expressed,
265 although an $α7_{EC1-5}/γC3_{EC6}$ chimera was included among the analytes to assess the role of α7 EC5
266 (Figure 4—figure supplement 1C). Each of the analytes was also analyzed by AUC to determine
267 their homophilic *cis*-interaction behavior (Figure 4—source data 1): Four analytes, $β1_{3-6}$, $γA4_{3-6}$,
268 $γA9_{3-6}$, and $γC3_{3-6}$, are monomeric in solution as measured by AUC, therefore their SPR binding
269 profiles could be analyzed to determine their heterophilic binding affinities (Figure 4B, Figure 4—
270 figure supplement 1A,B). For the remaining analytes, due to the added complexity of their
271 homophilic *cis* interactions in solution competing with their binding to the immobilized molecules,
272 the SPR responses could not be analyzed to determine accurate K_{DS} (Rich and Myszka, 2007).
273
274 The data clearly demonstrate a wide range of *cis* dimerization affinities with strong heterophilic
275 binding signals (500–2000 RU), with much weaker homophilic binding responses typically
276 between 100–140 RU. The strongest heterophilic *cis* interactions are in the sub-micromolar range;
277 for example, γC3/β9 can heterophilically *cis*-dimerize with a K_D of 0.22 μM, while $β9_{3-6}$, $γB2_{3-6}$,
278 $αC2_{2-6}$ and $γC5_{2-6}$ homodimerize with AUC-determined K_{DS} of 9–80 μM. In addition to uniformly
279 weak homophilic interactions, within-subfamily *cis* interactions were consistently among the
280 weakest observed although a number of inter-subfamily interactions were also relatively weak
281 (Figure 4A). For example, for the β9 surface comparatively weak binding was observed for all
282 tested β and γA isoforms except γA3, with the monomeric β1, γA4 and γA9 producing low
283 responses that could not be fit to a binding isotherm to calculate accurate K_{DS} (Figure 4B, Figure
284 4—figure supplement 1B). In contrast, robust binding to the β9 surface was observed for all γB

11

285   and C-type isoforms. These data are consistent with the binding responses when β9 was used as

286   an analyte over the other six surfaces, with weak to no binding observed over the γA4 and γA9

287   surfaces and robust responses over the γB2, αC2, γC3, and γC5 surfaces (Figure 4A). The γA4 and

288   γA9 surfaces showed a similar pattern of binding behaviors, with weak to no binding observed for

289   the γA and αC2 analytes, and robust binding for the γC-cPcdhs with K_{DS} for $\gamma C3_{3-6}$ of 2.73 and

290   9.60 μM respectively over each surface (Figure 4, Figure 4—figure supplement 1B).

291

292   Overall, these SPR data show that cPcdh *cis* binding is generally promiscuous, with measurable

293   *cis* interactions observed for 86% of pairs tested (using a 40 RU threshold). However, the wide range

294   of binding responses and homo- and hetero-dimeric K_{DS} that span 0.2201 μM to no measurable

295   interaction in solution suggests certain *cis* dimers will form preferentially to others. For the

296   heterophilic binding pairs for which K_{DS} could be determined (Figure 4B, Figure 4—figure

297   supplement 1, Figure 4—figure supplement 2), the alternate cPcdhs in particular, form markedly

298   stronger *cis* heterodimers with members of different subfamilies, particularly γC3 and/or γC5,

299   compared to their homodimeric and within-subfamily interactions. γC3 also formed stronger

300   heterodimers with αC2 than with itself or γC5. Of note, αC2 and γC5 both form strong *cis*

301   homodimers with K_{DS} of 8.9 μM and 18.4 μM respectively as determined from AUC experiments

302   (Figure 4—source data 1), a magnitude similar to many of their heterodimeric interactions of 11.5

303   μM and 6.9–18.2 μM respectively (Figure 4B).

304

305   In the next section we rationalize *cis* binding preferences in terms of the structural properties of

306   *cis* dimers.

307

308   ***The asymmetric cis dimer interface and cis binding specificity***

309   The crystal structure of the γB7 *cis* dimer revealed an asymmetric interaction, with the dimer

310   formed by one protomer engaging using surface of both EC5 and EC6 and one protomer engaging

311   using only EC6 (Goodman et al., 2017) with regions of EC6 overlapping in both EC5–6 and the

312   EC6-only interfaces for all cPcdh subfamilies (Thu et al., 2014; Goodman et al., 2017). The

313   asymmetric nature of the *cis* interaction implies that for each dimer interaction there are two

314   possible arrangements: one with protomer "1" forming the EC5–6 side and protomer "2" forming

315   the EC6-only side and the second where protomer "1" forms the EC6-only side and "2" the EC5–

316   6 side. These two configurations are distinct with different residue:residue interactions. Alternate

317   α-cPcdhs, which can only form the EC5–6 side of the *cis* dimer, require co-expression with a

318   "carrier" cPcdh from another cPcdh subfamily, which can form the EC6-only side of the *cis* dimer,

319   for robust delivery to the cell surface (Thu et al., 2014, Goodman et al., 2017). Although α-cPcdhs

320   and γC4, which also requires a carrier for delivery to the cell surface, are likely to be extreme

321   cases, sequence analysis alongside the low homodimerization ability of many cPcdh isoforms

322   suggests many cPcdhs will more readily form one side of the *cis* interface than the other (Goodman

323   et al., 2017).

324

325   We previously suggested that γA-cPcdhs will prefer to form the EC6-only side of the interface

326   since they have a poorly conserved EC5 interface and do not form strong homodimers in solution

327   (Figure 4—source data 1) (Goodman et al., 2017). The C-type cPcdh γC3 also does not form *cis*

328   homodimers in solution. However, as shown in Figure 4, γA-cPcdhs form strong heterodimers

329   with γC3 with dissociation constants in the low-micromolar range (Figure 4B and Figure 4—figure

330   supplement 1B). Structure-guided sequence analysis for the γA4/γC3 dimer in both EC6-only and

331   EC5–6 possible orientations, using the available crystal structures of the γB7$_{EC3–6}$ *cis* dimer and

332   monomeric γA4$_{EC3–6}$ (Figure 5A and Figure 5—figure supplement 1), suggests that γC3 prefers to

333   form the EC5–6 side: γC3 has a number of residue differences in interface residues that are

334   conserved among β, γA and γB cPcdhs (V/L555, R/K558, W/V562, and S/R595) that seem likely

335   to disfavor the EC6-only side of the interface and favor the EC5–6 side (Figure 5—figure

336   supplement 1B,C). Two of these residues, V555 and S595, result in a potential loss of EC6-only

337   interface buried surface area and are shared with α-cPcdhs, which cannot occupy the EC6-only

338   position (Goodman et al., 2017). Structural analysis further suggests that γC3-specific residue

339   R558 would not be well accommodated from the EC6-only side, potentially causing van der Waals

340   clashes (Figure 5—figure supplement 1C). By contrast, from the EC5–6 side R558 is positioned

341   to form an additional salt bridge with γA4 residue E544 and a hydrogen bond with Y532,

342   promoting dimer formation (Figure 5A; Figure 5—figure supplement 1B). γA4 residue E544 is

343   positioned to form this salt bridge due to the EC6 A/A' loop region adopting a different

344 arrangement in the γA4 crystal structure to that observed for γB2 and γB7 in their respective crystal

345 structures (Goodman et al., 2016c; Goodman et al., 2017).

346

347 Based on our analysis, we generated mutants of both γA4 and γC3 targeting the EC6-only side of

348 the interface and used size exclusion-coupled multi-angle light scattering (SEC-MALS) to assess

349 their preferred orientation on γA4/γC3 heterodimerization. In SEC-MALS wild type γA4$_{EC3–6}$ and

350 γC3$_{EC3–6}$ behave as monomers when run alone, and form a dimer when mixed in equimolar

351 amounts (Figure 5B; Figure 5—figure supplement 2A). The V560R mutation (γB7 numbering, see

352 methods for sequence alignment) is based on EC6-only impaired α-cPcdhs, and has been

353 previously shown to block γB6's homophilic *cis* interaction in solution (Goodman et al., 2017).

354 γA4 V560R did not dimerize with wild-type γC3, whereas γC3 V560R could still dimerize with

355 wild type γA4 (Figure 5B). Therefore impairing γA4's EC6-only interface blocks γA4/γC3 dimer

356 formation while impairing γC3's EC6-only interface does not (although the dimerization appears

357 to be weaker compared to the wild type γA4/γC3 *cis* interacting pairs). We also generated a γC3-

358 like mutant of γA4, K558R, which also targets the EC6-only interface. Like γA4 V560R, γA4

359 K558R also did not dimerize with wild type γC3 in MALS and, when replicated, in SPR

360 experiments (Figure 5B, Figure 5—figure supplement 2B). The reverse mutation in γC3, R558K,

361 inhibited dimerization with wild type γA4 (Figure 5B). Therefore, like the α-specific R560 residue,

362 γC3-specific R558 has distinct effects on dimerization when in γA4 or γC3, inhibiting

363 heterodimerization when mutated into γA4 but promoting heterodimerization in γC3. Together

364 these data suggest that the γA4/γC3 dimer has a preferred orientation, with γA4 predominantly

365 occupying the EC6-only position and γC3 the EC5–6 side. Our data also account for the fact that

366 neither isoform homodimerizes in solution since the EC5–6 side would be impaired in the γA4

367 homodimer while the EC6 side would be impaired in the γC3 homodimer.

368

369 Next, we sought to test whether γA4 and γC3 preferentially adopt these specific positions in *cis*

370 interactions with a γB isoform. To accomplish this we generated mutants of γB7 individually

371 targeting the EC6-only interaction surface, γB7 Y532G, and the EC5–6 side, γB7 A570R,

372 respectively (Goodman et al., 2017) (Figure 4—source data 1). In SPR, γB7 Y532G had only a

373 small impact on γA4 binding, while γB7 A570R abolished γA4 binding (Figure 5C). In contrast,

374 γB7 Y532G prevented γC3 binding while γB7 A570R showed robust γC3 binding (Figure 5C).

375 These results suggest that γA4/γB7 and γC3/γB7 *cis* heterodimers also have preferred orientations

376 with γA4 and γC3 maintaining their preferences for the EC6-only and EC5–6 positions

377 respectively. Additionally, SPR data for the γB7 mutants over the αC2 surface suggests αC2

378 preferentially occupies the EC6-only side in αC2/γB7 dimers (Figure 5C). This is notable since

379 αC2 forms robust *cis*-homodimers and therefore, like γB7, can presumably readily occupy both

380 positions in its homophilic interactions, implying that the αC2/γB7 orientation preference could

381 be specific to the particular heterodimer pairing. However, since this interpretation is based on a

382 single mutation further interrogation of αC2's interactions would be required to be conclusive. A

383 broader examination of orientation preferences among *cis* dimer pairings beyond those of

384 molecules with weak *cis* homodimer affinities, such as γA4 and γC3 examined here, could be

385 instructive.

386

387 **Discussion**

388 *Trans specificity* - The results of this study add to our current understanding of cPcdhs in a number

389 of ways. First, they reveal a remarkable level of specificity in *trans* homophilic interactions in the

390 sense that in no case was a heterophilic *trans* interaction detected in our SPR measurements. Prior

391 data has clearly indicated that cPcdhs exhibit a preference for homophilic *trans* interactions but

392 the extent of this specificity was not established in quantitative terms but were, rather, based on

393 cell aggregation experiments. The SPR experiments with cPcdhs reported here show no evidence

394 of cross-interaction between non-identical cPcdh isoforms. This level of specificity is unusual for

395 cell-cell recognition proteins, as significant intra-family interactions are evident in most other

396 families examined to date including type I cadherins (Katsamba et al., 2009; Vendome et al., 2014),

397 type II cadherins (Brasch et al., 2018), DIPs and Dprs (Cosmanescu et al., 2018), sidekicks

398 (Goodman et al., 2016c), and nectins (Harrison et al., 2012). Even the non-clustered δ-

399 protocadherins, which are preferentially homophilic and utilize an antiparallel EC1–4 interface

400 like the cPcdhs (Cooper et al., 2016; Harrison et al., 2020; Modak and Sotomayor, 2019), show

401   heterophilic intra-family *trans* interactions, though they show no cross-reactivity with cPcdhs

402   (Harrison et al., 2020).

403

404   High fidelity homophilic interaction is a strict requirement of the chain termination model for the

405   barcoding of vertebrate neurons and has been accomplished through the exploitation of a

406   multidomain interface of almost 4000 $Å^2$ (Nicoludis et al., 2019) that enables the positioning of

407   enough "negative constraints" (Sergeeva et al., 2020) to preclude the dimerization of about 1600

408   heterophilic pairs of 58 mouse cPcdh isoforms (Rubinstein et al., 2017). Dscams accomplish the

409   same task for thousands of isoforms by exploiting the combinatorics made possible by a three-

410   domain interface where each domain interacts largely independently with an identical domain on

411   its interacting partner (see discussion in (Zipursky and Grueber, 2013)). Although it is likely that

412   Dscams dimerize with a comparable level of homophilic specificity to that of cPcdhs, the evidence

413   is based on a semi-quantitative ELISA-type assay of recombinant multimerized isoforms

414   (Wojtowicz et al., 2007) and AUC experiments on a few select isoforms (Wu et al., 2012).

415

416   *Cis interactions* – Despite early evidence that *cis* interactions are promiscuous, the data reported

417   here indicate that this generalization needs to be significantly refined. Functional mutagenesis

418   studies have already established that alternate α cPcdhs and the C-type γC4 do not form intra-

419   subtype *cis* interactions and can only reach the cell surface when mediated by heterophilic *cis*

420   interactions with members of other subtype families (Goodman et al., 2017; Thu et al., 2014). The

421   data presented in Figure 4 indicate that this is an extreme example of quite general behavior: intra-

422   subtype *cis* interactions are invariably weaker than inter-subtype interactions. However, unlike α

423   cPcdhs, most cPcdhs can reach the cell surface on their own. This includes β1, all γA-Pcdhs, and

424   γC3 which do not form measurable homodimeric *cis* interactions in our solution-based AUC

425   experiments. We have attributed this to their presence on the restricted 2D surface of membranes

426   which can promote *cis*-dimerization (Wu et al., 2013) whereas biophysical experiments are carried

427   out in a 3D solution environment (Goodman et al., 2016b). (There may of course be other, still

428   undetermined, factors involved in cPcdh cell surface transport (Phillips et al., 2017).) Therefore,

429   although our biophysical experiments demonstrate that intra-subtype *cis* interactions are

430   comparatively weak and, in some cases undetectable in solution, intra-subtype *cis* dimers likely

431   assemble when constrained in more native membrane environments. As such, while α cPcdhs and

432   γC4 are obligate participants in *cis*-heterodimers, at least in their cell surface transport, our data

433   show that the remaining cPcdhs are preferentially, although not exclusively, participants in *cis*-

434   heterodimers.

435

436   The *cis* binding preferences indicated by our data can be largely understood in terms of the

437   asymmetric interface discussed above. Specifically, different isoforms preferentially form one side

438   of the *cis* dimer: for example, the EC6-only side for cPcdh-γA4 and the EC5–6 side for cPcdh-

439   γC3. Homodimerization requires participation of single isoform on both sides of an interface

440   posing challenges in the optimization of binding affinities since, in some cases, the same residue

441   must participate in different intermolecular interactions. Given significant sequence conservation

442   in all members of an alternate cPcdh subfamily (Figure 4—figure supplement 3) even intra-

443   subfamily heterophilic interactions are more difficult to optimize relative to inter-subfamily

444   heterodimerization where there are no constraints on the two interacting surfaces. Additionally,

445   the robust cell surface delivery of many cPcdhs in cells expressing only a single isoform also

446   suggests that all carrier isoforms – β-, γA-, and γB-cPcdhs, plus C-types αC2, γC3, and γC5 – can

447   fill both the EC6 and EC5–6 roles, as *cis*-dimer formation is thought to be required for cell surface

448   export (Goodman et al., 2017; Goodman et al., 2016b; Thu et al., 2014). Therefore side preferences

449   are most likely not absolute for carrier cPcdh isoforms and may vary among individual isoform

450   and/or subtype pairings.

451

452   *Functional implications of cPcdh interactions* – The functional role of precise *trans* homophilic

453   specificity in ensuring high fidelity discrimination between neuron self and non-self has been

454   discussed previously (Rubinstein et al., 2017; Rubinstein et al., 2015) and is summarized above. It

455   is an essential feature of the chain termination model. The role of promiscuous *cis* interactions can

456   also be understood in terms of this model in that *cis* promiscuity enables the formation of a large

457   and diverse set of *cis* dimers that can only form long molecular zippers when all isoforms are

458   matched. However, the results of this study reveal strong preferences for inter-subgroup

459   heterophilic interactions whose biological rationale is uncertain. cPcdhs from the three subfamilies

460   have been shown to act cooperatively in certain neuronal contexts although whether this relates to

461   their *cis* interactions is unknown (Hasegawa et al., 2016; Ing-Esteves et al., 2018).

462

463   One possible advantage of weak homophilic *cis* interactions would be to ensure that once reaching

464   the cell surface a diverse set of *cis* dimers forms. This explanation implicitly assumes that most

465   isoforms (except for α-Pcdhs and γC4) reach the surface as homodimers that must then quickly

466   dissociate and form more stable heterodimers. Another explanation posits that homotypic zippers

467   consisting solely of *cis*-homodimers are kinetically easier to form than heterotypic zippers since

468   in a homotypic zipper, either "wing" of the new *cis* dimer can form *trans* interactions with the

469   wing at the chain terminus. In contrast, in a hetero-dimeric zipper, only one wing can form

470   homophilic interactions with the chain terminus (Figure 1D). A preference for homotypic zippers

471   would then reduce the diversity required in the chain termination model since, in this model, it is

472   essential that all isoforms be incorporated into a growing zipper. The formation of long homotypic

473   zippers might lead to a repulsive phenotype even when mismatches are present.

474

475   However, these explanations would not fully account for interfamily heterophilic preferences. One

476   possibility is suggested by the observation that C-types are often highly expressed compared to

477   alternate cPcdhs, for example in Purkinje cells (Esumi et al., 2005; Kaneko et al., 2006). To ensure

478   sufficient diversity in growing zippers, it would then be important to ensure that zippers that are

479   formed are not overly enriched in C-type isoforms as would be accomplished through preferential

480   heterophilic *cis* interactions. This same logic would also pertain to alternate cPcdhs in cases where

481   one subfamily is more heavily expressed than another.

482

483   C-type cPcdhs have different functions than alternate cPcdhs and these are reflected in different

484   expression patterns. For example, αC2 can be alone responsible for tiling (Chen et al., 2017) (Of

485   note, in the chain termination model, a completely homophilic zipper is sufficient to initiate self-

486   avoidance facilitating tiling). On the other hand γC4, which has a unique and crucial role in

487   neuronal survival (Garrett et al., 2019), requires co-expression with another cPcdh isoform for

488   robust cell surface expression and therefore is likely unable to act in isolation (Thu et al., 2014).

489   Furthermore, as detailed above, γC4 has a much weaker *trans* interaction affinity than any other

490   cPcdh isoform measured to date, although it is still able to mediate cell aggregation when delivered

491   to the cell surface (Thu et al., 2014). The presence of E78 appears in large part to be responsible

492   for this weak affinity. It is unclear whether γC4's weak *trans* affinity plays any functional role,

493   although a weak homodimer interaction may facilitate extracellular interactions with other,

494   currently unidentified, proteins. More generally, it seems likely that different intracellular

495   interactions account for the specialized functions of C-type Pcdhs. The cytoplasmic domain plays

496   an important role in the activation of Wnt, WAVE, and other signaling cascades (Chen et al., 2009;

497   Fukuda et al., 2008; Keeler et al., 2015; Mah and Weiner, 2017; Onouchi et al., 2015; Pancho et

498   al., 2020). In some cases, the cytoplasmic domains of a subset or even a single cPcdh isoform

499   activates a specific signaling cascade. For example, cPcdh γC3 is the only isoform able to interact

500   and inhibit Axin1, a Wnt pathway activator (Mah et al., 2016). Of note, γ-cPcdh intracellular

501   domains consist of a C-terminal constant region common to all γ isoforms (including the three γ

502   C-types) and a membrane-proximal variable region consisting of ~100 residues that could account

503   for the unique intracellular interactions and signaling of individual isoforms. Additionally it is

504   possible that extracellular interactions to molecules from other families, such as Neuroligins, may

505   account for some distinctions in function (Molumby et al., 2017; Steffen et al., 2021).

506

507   Overall, the results of this study demonstrate the remarkable tuning of the interactions among

508   clustered protocadherin family members: homophilic *trans* interactions are remarkably specific

509   despite the high level of sequence identity among family members while *cis* interactions, though

510   somewhat promiscuous, also appear designed to have binding preferences of still uncertain

511   function. These binding properties match requirements of the "isoform-mismatch chain-

512   termination model" for neuronal self-vs-non-self discrimination in which all expressed cPcdh

513   isoforms assemble into intercellular zippers formed by alternating promiscuous *cis* and matched

514   *trans* interactions with assembly size dictated by the presence or absence of mismatched isoforms.

515   It remains to be seen whether such assemblies can be observed *in vivo* and how they control

516   downstream signaling pathways.

517

Materials and Methods

Protein production and purification

cDNAs for mouse cPcdh ectodomain fragments, excluding the predicted signal sequences, were cloned into a pαSHP-H mammalian expression vector (a kind gift from Daniel J. Leahy, John Hopkins University) modified with the human Binding immunoglobulin protein (BiP; MKLSLVAAMLLLLSAARA) signal sequence and a C-terminal octa-histidine tag (Rubinstein et al., 2015). The signal sequences were predicted using the SignalP 4.0 server (Petersen et al., 2011). Point mutations were introduced into cDNA constructs using the KOD hot start polymerase (Novagen) following the standard Quikchange protocol (Stratagene).

Suspension-adapted HEK293 Freestyle cells (Invitrogen) in serum free media (Invitrogen) grown and maintained at 37 °C and 10% carbon dioxide were used for protein expression. FreeStyle™ 293-F cell line has been authenticated and verified negative for mycoplasma using PCR testing (ThermoFisher). The plasmid constructs were transfected into cells using polyethyleneimine (Polysciences Inc.) (Baldi et al., 2012). Media was supplemented with 10 mM $CaCl_2$ 4 hours after transfection. Conditioned media was harvested ~6 days after transfection and the secreted proteins were purified using batch nickel-nitrilotriacetic acid (Ni-NTA) affinity chromatography followed by size exclusion chromatography over Superdex 200 26/60 column (Cytiva) on an AKTA pure fast protein liquid chromatography system (Cytiva). Purified proteins were concentrated to >2 mg/ml in 10 mM Tris-Cl pH 8.0, 150 mM NaCl, 3 mM $CaCl_2$, and 100–250 mM imidazole pH 8.0 and stored at 4 °C for short-term use or flash frozen in liquid nitrogen for long-term storage at –80 °C.

Constructs encoding biotinylated cPcdh fragments for immobilization in SPR experiments were prepared by insertion of an Avi-tag (GLNDIFEAQKIEWHE)-encoding sequence between the octa-histidine tag and stop codon. These were co-transfected with a plasmid encoding the biotin-Ligase BirA from E. coli (Lys2–Lys321) with a BiP signal sequence and a C-terminal endoplasmic reticulum-retention signal (DYKDEL) (Barat and Wu, 2007). The expression and BirA plasmids were mixed at a 9:1 ratio for transfection and 50 μM Biotin (Sigma) was added to the media 4 h post-transfection. Purification was carried out exactly as for the non-biotinylated constructs and biotinylation was confirmed by western blot using NeutrAvidin-HRP (ThermoFisher).

549

Sedimentation equilibrium analytical ultracentrifugation (AUC)

Protein	Imidazole pH 8.0 (mM)	Spin speeds (rpm)
α4 EC1–5	100	9000, 11000, 13000, 15000
α7 EC1–5 L301R	100	9000, 11000, 13000, 15000
α12 EC1–5 *(poorly behaved)*	200	11000, 14000, 17000, 20000
γB4 EC1–5	200	11000, 14000, 17000, 20000
γB5 EC1–4-AVI	200	11000, 14000, 17000, 20000
γC5 EC1–5 S116R	200	11000, 14000, 17000, 20000
β6 EC1–4	100	9000, 11000, 13000, 15000
β6 EC1–4-AVI tag	200	11000, 14000, 17000, 20000
β6 EC1–4 R41N	200	11000, 14000, 17000, 20000
β6 EC1–4 S117I	200	11000, 14000, 17000, 20000
β6 EC1–4 L125P	200	11000, 14000, 17000, 20000
β6 EC1–4 E369K	200	11000, 14000, 17000, 20000
β6 EC1–4 Y371F	200	11000, 14000, 17000, 20000
β6 EC1–4 R41N/S117I *(precipitates)*	200	11000, 14000, 17000, 20000
β6 EC1–4 R41N/E369K	200	11000, 14000, 17000, 20000
β6 EC1–4 S117I/L125P	200	11000, 14000, 17000, 20000
β6 EC1–4 R41N/S117I/L125P	200	11000, 14000, 17000, 20000
β6 EC1–4 R41N/S117I/E369K	200	11000, 14000, 17000, 20000
β6 EC1–4 R41N/E369K/Y371F	200	11000, 14000, 17000, 20000
β6 EC1–4 R41N/S117I/L125P/ E369K/Y371F	200	11000, 14000, 17000, 20000
β1 EC3–6	200	12000, 16000, 20000, 24000
β6 EC1–6	250	9000, 11000, 13000, 15000
β9 EC3–6	200	11000, 14000, 17000, 20000
γA3 EC3–6	200	11000, 14000, 17000, 20000
γA9 EC3–6	200	11000, 14000, 17000, 20000
γB7 EC3–6 A570R	200	13000, 17000, 21000, 25000
αC2 EC3–6-AVI tag	200	11000, 14000, 17000, 20000
γC5 EC2–6	250	9000, 11000, 13000, 15000
γC4 EC1–4	250	11000, 14000, 17000, 20000
γC4 EC1–4 D290A	250	11000, 14000, 17000, 20000
γC4 EC1–4 D290N	250	11000, 14000, 17000, 20000
γC4 EC1–4 E78A	250	11000, 14000, 17000, 20000
γC4 EC1–4 E78Q	250	11000, 14000, 17000, 20000
γC4 EC1–4 S344R	250	11000, 14000, 17000, 20000

551 Experiments were performed in a Beckman XL-A/I analytical ultracentrifuge (Beckman-Coulter,

552 Palo Alto CA, USA), utilizing six-cell centerpieces with straight walls, 12 mm path length and

553 sapphire windows. Protein samples were dialyzed overnight and then diluted in 10 mM Tris-Cl

554 pH 8.0, 150 mM NaCl, 3 mM CaCl$_2$ with 100–250 mM imidazole pH 8.0, as detailed in the above

555 table. The samples were diluted to an absorbance of 0.65, 0.43 and 0.23 at 10 mm and 280 nm in

556 channels A, B and C, respectively. For each sample, buffer was used as blank. The samples were

557 run in duplicate at four speeds as detailed in the above table. The lowest speed was held for 20 h
558 then four scans were conducted with 1 h interval, the subsequent three speeds were each held for
559 10 h followed by four scans with 1 hour interval each. Measurements were taken at 25 °C, and
560 detection was by UV at 280 nm or interference. Solvent density and protein v-bar at both
561 temperatures were determined using the program SednTerp (Alliance Protein Laboratories, Corte
562 Cancion, Thousand Oaks, CA, USA). The molecular weight of each protomer used in AUC
563 experiments, was determined by MALDI mass spectrometry. For calculation of dimeric K_D and
564 apparent molecular weight, all data were used in a global fit, using the program HeteroAnalysis,
565 (www.biotech.uconn.edu/auf). Calculation of the tetramer K_ds was done with the program Sedphat
566 (http://www.analyticalultracentrifugation.com/sedphat/index.htm).

567

568 **Surface plasmon resonance (SPR) binding experiments**
569 SPR binding experiments were performed using a Biacore T100 biosensor equipped with a Series
570 S CM4 sensor chip, immobilized with NeutrAvidin over all four flow cells. NeutrAvidin
571 immobilization was performed in HBS-P buffer, pH 7.4 at 32 °C, over all four surfaces using
572 amine-coupling chemistry as described in Katsamba et al. (2009), resulting in approximately
573 10,000 RU of NeutrAvidin immobilized (Katsamba et al., 2009). Binding experiments were
574 performed at 25 °C in a running buffer containing 10 mM Tris-Cl pH 8.0, 150 mM NaCl, 3 mM
575 CaCl$_2$, 20 mM imidazole, 0.25 mg/mL BSA and 0.005% (v/v) Tween-20 unless otherwise noted.

576

577 C-terminal biotinylated fragments were tethered over individual NeutrAvidin-immobilized flow
578 cells (shown in the left column of each Figures 2, 4, 5C, Figure 2—figure supplement 1, Figure
579 2—figure supplement 2B, Figure 4—figure supplement 1 and Figure 5—figure supplement 2B) at
580 2300–3000 RU, depending on the experiment, using a flow rate of 20 μL/min. A NeutrAvidin-
581 immobilized flow cell was used as a reference in each experiment to subtract bulk refractive index
582 changes. The analytes tested in each experiment are listed at the top row. All analytes (with
583 exceptions for the *cis* interacting pairs γC3$_{3-6}$/β9$_{3-6}$, in both orientations, and β6$_{1-6}$/γC3$_{3-6}$ in Figure
584 4A, discussed below) were tested at six concentrations ranging between 24, 8, 2.667, 0.889, 0.296,
585 and 0.099 μM, prepared using a three-fold dilution series. γC3$_{3-6}$ binding over β9$_{3-6}$ (Figure 4A)
586 was tested at five concentrations from 8–0.099 μM.

587   For all experiments, analyte samples were injected over the captured surfaces at 50 μL/min for 40

588   s, followed by 180 s of dissociation phase, a running buffer wash step and a buffer injection at 100

589   μL/min for 60 s. Protein samples were tested in order of increasing concentration, and within the

590   same experiment the entire concentration series was repeated to confirm reproducibility. Every

591   three binding cycles, buffer was used as an analyte instead of a protein sample to double reference

592   the binding responses by removing systematic noise and instrument drift. The resulting binding

593   curves were normalized for molecular weight differences according to data provided by mass spec

594   for each molecule. The data was processed using Scrubber 2.0 (BioLogic Software). To provide

595   an estimate of the number of possible heterophilic binding pairs, we have used a cut-off of 40RU,

596   which is the lowest signal that can be observed for a homodimeric *cis* fragment pair, γB2$_{3-6}$.

597

598   In Figure 4A, β6$_{1-6}$ and β9$_{3-6}$ were tested over γC3$_{3-6}$ at six concentrations ranging from 900 to 3.7

599   nM, which is 27-fold lower than the other interactions, prepared using a three-fold dilution series

600   in a running buffer containing increased concentrations of imidazole (100 mM) and BSA (0.5

601   mg/mL) to minimize nonspecific interactions. For these two interactions, although analyte samples

602   were injected over the captured surfaces at 50 μL/min for 40s, the dissociation phase was

603   monitored for 300s to provide additional time for complex dissociation. Nevertheless, higher

604   analyte concentrations produced binding profiles that were not reproducible, most likely due to the

605   fact that bound complexes could not dissociate completely at these higher concentrations.

606

607   For the calculation of heterophilic K$_{DS}$ for the monomeric *cis* fragments β1$_{3-6}$, γA4$_{3-6}$, γA9$_{3-6}$ and

608   γC3$_{3-6}$ over each of the six surfaces, except β9$_{3-6}$, the duplicate binding responses were fit globally,

609   using an 1:1 interaction model and a single K$_D$ was calculated as the analyte concentration that

610   would yield 0.5 R$_{max}$ and a fitting error, indicated in brackets. K$_{DS}$ lower than 24 μM were

611   calculated using an independent R$_{max}$. For K$_{DS}$ greater 24 μM, the R$_{max}$ was fixed to a global value

612   determined by the R$_{max}$ of a different cPcdh analyte tested over the same surface during the same

613   experiment that showed binding above 50% and therefore produced a more accurate R$_{max}$. For K$_{DS}$

614   >50 μM, a lower limit is listed since at the analyte concentrations used, (0.098-24 μM), accurate

615   K$_{DS}$ could not be determined, even when the R$_{max}$ is fixed. NB (No Binding) represents

616   interactions that did not yield any binding signal. The binding curves of γC3$_{3-6}$ over the β9$_{3-6}$ did

617   not come to equilibrium during the time-course of the experiment, so a kinetic analysis was

618   performed to calculate a K_D (Figure 4—figure supplement 1A). Binding of $\gamma C3_{3-6}$ was tested using

619   a concentration range of 900–0.411 nM prepared using a three-fold dilution series in a running

620   buffer containing increased concentrations or imidazole (100 mM) and BSA (0.5 mg/mL) to

621   minimize any nonspecific interactions. Protein samples were injected over the captured surfaces

622   at 50 µL/min for 90 s, followed by 420 s of dissociation phase, a running buffer wash step and a

623   buffer injection at 100 µL/min for 60 s. Protein samples were tested in order of increasing

624   concentration in triplicate to confirm reproducibility. Every three binding cycles, buffer was used

625   as an analyte instead of a protein sample to double reference the binding responses by removing

626   systematic noise and instrument drift. The binding data was analyzed using an 1:1 interaction

627   model to calculate the kinetic parameters and the K_D.

628

629   **K562 cell aggregation assays**

630   Full-length cPcdhs β6 and β8 cDNAs were cloned into the pMax expression vectors encoding C-

631   terminal mCherry or mVenus tagged cPcdh proteins, then transfected into K562 cells (ATCC

632   CCL243) as previously described (Goodman et al., 2017; Thu et al., 2014). K-562 bone marrow

633   chronic myelogenous leukemia (CML) cell line has been authenticated and verified negative for

634   mycoplasma using PCR testing (ATCC). Point mutants were generated using the QuikChange

635   method (Stratagene). In brief, K562 cells were cultured at 37 °C with 5% CO_2 in DMEM with

636   GlutaMAX (GIBCO) supplemented with 10% FBS and 1% penicillin-streptomycin for two days.

637   Next, cells were counted, centrifuged, and resuspended at a density of $\sim1.5\times10^4$ cells/µL in SF

638   Cell Line 4D-Nucleofector Solution SF with supplement according to manufacturer instructions

639   (Lonza). 2 µg of each Pcdh expression construct were transfected into 20 µL of the K562 cell

640   suspension by electroporation using an Amaxa 4D-Nucleofector (Lonza). Transfected cells were

641   transferred to a 24-well plate in 500 µL of medium per well and incubated overnight at 37°C and

642   5% CO_2. Cells then were mixed, re-incubated with gentle rocking for 4 hours, then imaged with

643   an Olympus IX73 fluorescent microscope to determine the extent of aggregation.

644

645   **Size-exclusion coupled multi-angle light scattering (SEC–MALS)**

646   SEC-MALS experiments were performed using a Superdex 200 Increase 3.2/300 size exclusion

647   column on an AKTA FPLC system (Cytiva) coupled to inline static light scattering (Dawn Heleos

648   II, Wyatt Technology), differential refractive index (Optilab rEX, Wyatt Technology) and UV

649   detection. Purified cPcdh proteins were diluted to 18 μM in running buffer (150 mM NaCl, 10 mM

650   Tris-Cl pH 8, 3 mM $CaCl_2$, 200 mM Imidazole pH 8) and 50 or 100 μl samples were run at a flow

651   rate of 0.5 ml/min at room temperature. Mixtures of cPcdh fragments were prepared in the same

652   buffer at final concentrations of 18 μM for each protein and run under the same conditions. Data

653   were analyzed using ASTRA software (Wyatt Technologies).

654

655   During SEC-MALS experiments, a dimer/monomer equilibrium is established as proteins move

656   through the size exclusion chromatography column, which is influenced by the K_D of the

657   interaction. The concentrations used in the current experiments (18 μM for each cPcdh fragment),

658   although above the K_D of 3 μM for the γC3/γA4 *cis* interaction, are not sufficiently high for all the

659   *cis* fragments to be bound into heterodimers, leaving a significant population of molecules as

660   monomers, resulting in apparent molecular weights of ~76 kDa for the dimeric species compared

661   to the predicted molecular weight for a dimer of ~108 kDa.

662

663   **X-ray crystallography**

664   Crystallization screening of γC4$_{1-4}$ using the vapor diffusion method yielded two protein crystal

665   forms: The first crystal form crystals were grown using a protein concentration of 7 mg/ml in 10%

666   (w/v) PEG8000, 20% ethylene glycol, 10% Morpheus Amino Acids (Molecular Dimensions), and

667   0.1 M Morpheus Buffer System 2 (Hepes/MOPS buffer; Molecular Dimensions) pH 7.5. No

668   additional cryoprotection was required for this crystal form. The second crystal form crystals were

669   grown using a protein concentration of 7 mg/ml in 1 M LiCl, 0.1 M Mes pH 6.0, and 10% (w/v)

670   PEG6000. The crystal used for data collection was cryo-protected in the crystallization condition

671   plus 30% (w/v) glycerol. X-ray diffraction data for each crystal form were collected at 100K from

672   single crystals at Northeastern Collaborative Access Team (NE-CAT) beamline 24ID-E at the

673   Advanced Photon Source, Argonne National Laboratory.

674

675   *γC4$_{1-4}$ crystal form 1: Diffraction anisotropy and pseudosymmetry*

676   The X-ray diffraction data for the first crystal form showed strong diffraction anisotropy, with

677   relatively strong diffraction along c* and much weaker diffraction along a* and b* (Figure 3—

678   figure supplement 1A). These data were therefore truncated using ellipsoidal limits with using a

679   3.0 F/sigma cut-off along each of the three principal crystal axes as implemented in the UCLA

680   Diffraction Anisotropy Server (Strong et al., 2006) to 4.6/3.9/3.5 Å. The completeness within the

681   applied ellipsoidal resolution limits was 96.8% (Figure 3—source data 1).

682

683   ***$\gamma C4_{1-4}$ crystal form 1: Crystal structure phasing and refinement***

684   The $\gamma C4_{1-4}$ crystal structure was solved by molecular replacement using Phaser (McCoy et al.,

685   2007), implemented in CCP4 (Winn et al., 2011). The $\gamma C5_{EC1-3}$ crystal structure (PDB: 4ZPO)

686   modified using a sequence alignment to $\gamma C4$ with Phenix's MRage program (Liebschner et al.,

687   2019) was used as a search model. Following an initial round of rigid body refinement in Phenix

688   (Liebschner et al., 2019) the EC domain 4 from the $\alpha 7_{EC1-5}$ crystal structure (PDB: 5DZV) was

689   manually placed into the electron density map, using structural alignment to the EC1–3 regions as

690   a guide. The resulting model was subjected to a further round of rigid body refinement. At this

691   stage there was clear difference density for the interdomain calcium ions and covalently linked

692   glycans not present in the models. Iterative model building using Coot (Emsley et al., 2010) and

693   maximum-likelihood refinement using Phenix (Liebschner et al., 2019) was subsequently

694   conducted. The higher resolution (2.4 Å) crystal form 2 crystal structure (see below) was used as

695   a reference model in later rounds of iterative model-building and refinement to guide the local

696   geometry choices in this lower resolution structure. Final refinement statistics are given in Figure

697   3—source data 1.

698

699   ***$\gamma C4_{1-4}$ crystal form 2: data processing, phasing, and refinement***

700   The $\gamma C4_{1-4}$ crystal form 2 dataset was indexed using XDS (Kabsch, 2010) and scaled using

701   AIMLESS (Evans and Murshudov, 2013). The data was spherically truncated with high resolution

702   limit of 2.4 Å. Data collection statistics are given in Figure 3—source data 1.

703

704   The $\gamma C4_{1-4}$ crystal form 2 crystal structure has two molecules in the asymmetric unit was solved

705   by molecular replacement using Phaser (McCoy et al., 2007), implemented in Phenix (Liebschner

706   et al., 2019), using the EC2–3 portion of the *trans*-dimer from the crystal form 1 crystal structure

707   early in refinement as a search model. The molecular replacement solution was then subjected to

708   an initial round of rigid body refinement using Phenix, followed by two rounds of model building

709   in Coot (Emsley et al., 2010) and maximum likelihood refinement in Phenix. The two EC4

710   domains were then manually placed in the electron density and subjected to rigid body refinement.

711   Following a further two iterative rounds of model building and refinement the two EC1 domains

712   were manually placed. Iterative model-building and refinement continued yielding the final crystal

713   structure whose statistics are given in Figure 3—source data 1.

714

715   **Structure analysis**

716   Buried surface areas were calculated using 'Protein interfaces, surfaces and assemblies' service

717   (PISA) at the European Bioinformatics Institute (http://www.ebi.ac.uk/pdbe/prot_int/pistart.html)

718   (Krissinel and Henrick, 2007) and are given as the change in accessible surface area over both

719   protomers. Root mean square deviations over aligned Cα atoms (RMSDs) between structures were

720   calculated using Pymol (Schrödinger, LLC). Crystal structure figures were made using Pymol

721   (Schrödinger, LLC).

722

723   **Sequence analysis**

724   Multiple sequence alignments were generated using Clustal Omega (Sievers et al., 2011) and

725   visualized using ESPript3.0 (Robert and Gouet, 2014). Sequence logos were generated from

726   multiple sequence alignments using WebLogo3 (Crooks et al., 2004).

727

728   ***Amino acid sequence alignment of cPcdhs γB7, γA4, and γC3 EC1–6 regions***

```
729   CLUSTAL O(1.2.4) multiple sequence alignment
730
731   γB7     -QPVRYSIPEELDRGSVVGKLAKDLGLSVLEVSARKLRVS--AEKLHFSVDSESGDLLVK      57
732   γA4     -EQIRYSVPEELERGSVVGNLAADLGLEPGKLAERGVRIVSRGKTQLFALNPRSGSLVTA      59
733   γC3     STIIHYEILEERERGFPVGNVVTDLGLDLGSLSARRLRVVSGASRRFFEVNWETGEMFVN      60
734            ::*.: ** :** **::. ****.  .:: * :*:   ..   * :: .:*.:..
735
736   γB7     DRIDREQICKGRRKCELQLEAVLENPLNIFHVVVEIEDVNDHAPQFPKDEINLEISESDS     117
737   γA4     GRVDREGLCDRSPKCTANLEILLEDKVRILAIEVEIIDVNDNAPSFGAQQREIKVAESEN     119
738   γC3     DRLDREELCGTLPSCTVTLELVVENPLELFSAEVVVQDINDNNPSFPTGEMKLEISEALA     120
739            .*:*** :*    .*   ** ::*: :.::   * : *:**: *.*    : :::::*:
740
741   γB7     PGARTILESAKDLDIGMNSLSKYQLSPNDYFLLLVKDNPDGSKYPELELQKMLDREAEST     177
742   γA4     PGTRFPLPEAFDLDIGVNALQGYQLSSNDHFSLDVQSGPDGIKYPELVLENALDREEEAV     179
743   γC3     PGTRFPLESAHDPDVGSNSLQTYELSHNEYFALRVQTREDGTKYAELVLERALDWEREPS     180
744            **:*   * .* * *:* *:*. *:** *::* * *:   ** ** ** *:. ** * *
745
746   γB7     HHLMLTAVDGGDPPRTGTTQLRIRVVDANDNRPVFSQDVYRVRLPEDLPPGTTVLRLKAM     237
747   γA4     HHLVLTAFDGGDPVRSGTATIQVTLVDTNDNAPVFTQPEYHISVKENLPVGTRLLTIKAT     239
748   γC3     VQLVLTALDGGTPARSATLPIRITVLDANDNAPAFNQSLYRARVREDAPPGTRVAQVLAT     240
749            :*:***.*** * *:.*   ::: ::*:*** *.*.*  *:   : *: * **  :  : *
750
```

```
751   γB7   DQDEGINAEFTYSFLGV-ANK--AQFSLDPITGDIVTRQSLDFEEVEQYTIDVEAKDRGS   294
752   γA4   DPDEGVNGEVTYSFRNV-REKISQLFQLNSLTGDITVLGELDYEDSGFYDVDVEAHDGPG   298
753   γC3   DLDEGLNGEIVYSFGSHNRAGVRELFALDLVTGVLTIKGRLDFEDTKLHEIYIQAKDKGA   300
754         * ***:*.*..*** .           * *: :** :.     **:*:   : : ::*:*   .
755
756   γB7   --LSSQCKVIIEVLDENDNRPEIIITSLSDQISEDSPSGTVVALFKVRDRDSGENAEVMC   352
757   γA4   --LRARSKVLVTVLDVNDNAPEVTVTSLTSSIQEASSPGTVIALFNVHDSDSGENGLVTC   356
758   γC3   NPEGAHCKVLVEVVDVNDNAPEITVTSVYSPVPEDAPLGTVIALLSVTDLDAGENGLVTC   360
759         ::.**:: *:* *** **: :**: . : * :  ***:**:.* * *:***. * *
760
761   γB7   SLSGNNPFKIHSSSNNYYKLVTDSILDREQTPGYNVTITATDRGKPPLSSSTTITLNVAD   412
762   γA4   SIPDNLPFRLEKTYGNYHRLLIHRTLDREEVSDYNITITATDQGTPPLSTETYISLQVVD   416
763   γC3   EVPPGLPFSLTSSLKNYFTLKTSAALDRETMPEYNLSITARDSGIPSLSALTTVKVQVSD   420
764         .: . ** : .: **. *     **** **::*** * * * **: * :..::* *
765
766   γB7   VNDNAPVFQQQAYLINVAENNQPGTSITQVKAWDPDVGSNGLVSYSIIASDLEPKALSSF   472
767   γA4   INDNPPTFTHASYSAYIPENNPRGASILSITAQDPDSGENAQVIYSLSEDTIQGAPMSSY   476
768   γC3   INDNPPQSSQSSYDVYVEENNLPGVPILNLSVWDPDAPPNARLSFFLLEPGAETGLVSRY   480
769         :*** *   : :*   :  ***  *. *  .:.. ***   *. : : :     :   :* :
770
771   γB7   VSVNQDSGVVYAQRAFDHEQIRSFQLTLQARDQGSPALSANVSMRVLVDDRNDNAPRVLY   532
772   γA4   VSINSNTGVLYALRSFDYEQFQDLKLLVTARDSGTPPLSSNVSLSLSVLDQNDNTPEILY   536
773   γC3   FTINRDNGVLTTLVPLDYEDQREFQLTAHINDGGTPVLATNISVNVFVTDRNDNAPQVLY   540
774         .::* :.**: :   :*:*: :.::*    .* *:* *::*:*: : * *:***:*.:**
775
776   γB7   PTLEPDGSALFDMVPRAAEPGYLVTKVVAVDADSGHNAWLSYHVLQASDPGLFSLGLRTG   592
777   γA4   PTIPTDGSTGVELTPRSADPGYLVTKVVAVDKDSGQNAWLSYRLLKASEPGLFSVGLHTG   596
778   γC3   PR---PGQSSVEMLPRGTAAGHVVSRVVGWDADAGHNAWLSYSLLGAPNQSLFAVGLHTG   597
779         *     *.: .:: **.: *::*::**. * *:*:***** :* * : .**:*:**:**
780
781   γB7   EVRTARALSDKDAARQRLLVAVRDGGQPPLSATATLLLVFADSLQE   638
782   γA4   EVRTARALLDRDALKQSLVVTVQDHGQPPLSATVTLTIAVSDNIPD   642
783   γC3   QISTARPIQDTDSPRQILTVLISDSGEPLLSTTATLTVSVTEESPE   643
784         :: *** : * *: :* * * : * *:* **:*.** : .::. :
785
```

Structure-based sequence analysis of the γA4/γC3 interaction

Since both γA4$_{3-6}$ and γC3$_{3-6}$ are monomeric in solution but form a robust heterodimer when mixed (in SPR, AUC, and SEC-MALS) we hypothesized that these molecules might have opposing *cis* interaction side preferences. To facilitate hypothesis generation on the nature of their *cis* heterodimer interaction we modeled the two possible γA4/γC3 *cis* dimers: one with γA4 occupying the EC6-only position and γC3 the EC5–6 position; and the second with γC3 in the EC6-only position and γA4 in the EC5–6 position. To do this the monomeric γA4$_{EC3-6}$ crystal structure (PDB: 5SZQ) was structurally superimposed over EC6 domains with the EC6-only protomer from the γB7$_{EC3-6}$ *cis*-dimer crystal structure (PDB: 5V5X; RMSD 0.7 Å over 91 aligned Cαs) or over EC5–6 domains with the EC5–6 protomer (RMSD 1.0 Å over 194 aligned Cαs). Since γA4 and γB7 are so structurally similar in their EC5–6 regions modeling γA4's *cis* interactions in this manner as a

797 basis for hypothesis generation seemed reasonable. The only region of significant structural
798 deviation within the EC5–6 regions between γA4 and γB7 is in the EC6 A–A' loop region which
799 has a peripheral role in the EC6-only protomer interface. For modelling γC3 we used
800 computational mutagenesis of the γB7 structure selecting the best-fit rotamer for each amino acid
801 from the Dunbrack rotamer library (Shapovalov and Dunbrack, 2011), implemented in UCSF
802 Chimera (Pettersen et al., 2004). No energy minimization was conducted and the models are
803 intended only for use in hypothesis generation.
804
805 ***Cis interface mutants***
806 Our studies of Pcdh *cis* interactions we have found that mutagenesis of the *cis* interface commonly
807 has a deleterious impact on protein expression levels in our system (Goodman et al., 2017). We
808 assume this is because *cis* interaction is required for robust cell-surface delivery/secretion (Thu et
809 al., 2014), although this hasn't been specifically addressed in our HEK293 protein expression
810 system.
811
812 To test our structure-guided hypotheses regarding γA4 and γC3s' *cis* interactions and side
813 preferences as we tried to make a number of different *cis* interface mutants and were able to obtain
814 four different mutants (see table below). Since protein yields were generally too low for AUC and
815 SPR, MALS was used to study the impact of these mutants on γA4/γC3 *cis* dimer formation.
816

Mutant protein (γB7 numbering given in parentheses)	Cis interface side targeted	Protein expression in 25 mL test
γC3 EC3–6 Y540G (Y532G equivalent)	EC6-only	No
γC3 EC3–6 V560D (L555D equivalent)	EC6-only	No
γC3 EC3–6 V565R (V560R equivalent)	EC6-only	Yes
γC3 EC3–6 A575R (A570R equivalent)	EC5–6	No
γC3 EC3–6 R563K (K558R equivalent)	Both	Yes
γA4 EC3–6 Y536G (Y532G equivalent)	EC6-only	No
γA4 EC3–6 L559D (L555D equivalent)	EC6-only	No
γA4 EC3–6 V564R (V560R equivalent)	EC6-only	Yes
γA4 EC3–6 A574R (A570R equivalent)	EC5–6	No
γA4 EC3–6 K562R (K558R equivalent)	EC6-only	Yes
β1 EC3–6 V563R (V560R equivalent)	EC6-only	No
β1 EC3–6 S573R (A570R equivalent)	EC6-only	No
β1 EC3–6 K561R (K558R equivalent)	EC5–6	No
β9 EC3–6 V563R (V560R equivalent)	EC6-only	No
β9 EC3–6 A573R (A570R equivalent)	EC6-only	No
β9 EC3–6 K561R (K558R equivalent)	EC5–6	No

817

818 **Accession numbers**

819 Atomic coordinates and structure factors for the γC4 EC1–4 crystal structures are deposited in the

820 protein data bank with accession codes PDB: 7JGZ and 7RGF.

821 **Acknowledgements**

828 **Competing Interests**

829 The authors declare no competing interests.

830 **Supplementary Files**

831   Figure 2—figure supplements 1–2 and source data 1

832   Figure 3—figure supplement 1 and source data 1–2

833   Figure 4—figure supplements 1–3 and source data 1

834   Figure 5—figure supplements 1–2

835 **References**

836 Baldi, L., Hacker, D.L., Meerschman, C., and Wurm, F.M. (2012). Large-Scale Transfection of Mammalian
837 Cells. In Protein Expression in Mammalian Cells: Methods and Protocols, J.L. Hartley, ed. (Totowa, NJ:
838 Humana Press), pp. 13-26.

839 Barat, B., and Wu, A.M. (2007). Metabolic biotinylation of recombinant antibody by biotin ligase retained
840 in the endoplasmic reticulum. Biomolecular Engineering *24*, 283-291.

841 Bonn, S., Seeburg, P.H., and Schwarz, M.K. (2007). Combinatorial Expression of α- and γ-Protocadherins
842 Alters Their Presenilin-Dependent Processing. Molecular and Cellular Biology *27*, 4121-4132.

843 Brasch, J., Goodman, K.M., Noble, A.J., Rapp, M., Mannepalli, S., Bahna, F., Dandey, V.P., Bepler, T.,
844 Berger, B., Maniatis, T.*, et al.* (2019). Visualization of clustered protocadherin neuronal self-recognition
845 complexes. Nature *569*, 280-283.

846 Brasch, J., Katsamba, P.S., Harrison, O.J., Ahlsén, G., Troyanovsky, R.B., Indra, I., Kaczynska, A., Kaeser,
847 B., Troyanovsky, S., Honig, B.*, et al.* (2018). Homophilic and Heterophilic Interactions of Type II
848 Cadherins Identify Specificity Groups Underlying Cell-Adhesive Behavior. Cell Reports *23*, 1840-1852.

849 Canzio, D., and Maniatis, T. (2019). The generation of a protocadherin cell-surface recognition code for
850 neural circuit assembly. Current Opinion in Neurobiology *59*, 213-220.

851 Chen, J., Lu, Y., Meng, S., Han, M.-H., Lin, C., and Wang, X. (2009). α- and γ-Protocadherins Negatively
852 Regulate PYK2. Journal of Biological Chemistry *284*, 2880-2890.

853 Chen, W.V., Nwakeze, C.L., Denny, C.A., O'Keeffe, S., Rieger, M.A., Mountoufaris, G., Kirner, A.,
854 Dougherty, J.D., Hen, R., Wu, Q.*, et al.* (2017). Pcdhαc2 is required for axonal tiling and assembly of
855 serotonergic circuitries in mice. Science *356*, 406-411.

856 Cooper, S.R., Jontes, J.D., and Sotomayor, M. (2016). Structural determinants of adhesion by
857 Protocadherin-19 and implications for its role in epilepsy. eLife *5*, e18529.

858 Cosmanescu, F., Katsamba, P.S., Sergeeva, A.P., Ahlsen, G., Patel, S.D., Brewer, J.J., Tan, L., Xu, S., Xiao,
859 Q., Nagarkar-Jaiswal, S.*, et al.* (2018). Neuron-Subtype-Specific Expression, Interaction Affinities, and
860 Specificity Determinants of DIP/Dpr Cell Recognition Proteins. Neuron *100*, 1385-1400.e1386.

861 Crooks, G.E., Hon, G., Chandonia, J.-M., and Brenner, S.E. (2004). WebLogo: A Sequence Logo
862 Generator. Genome Research *14*, 1188-1190.

863 Emsley, P., Lohkamp, B., Scott, W.G., and Cowtan, K. (2010). Features and development of Coot. Acta
864 Crystallographica Section D: Biological Crystallography *66*, 486-501.

865   Esumi, S., Kakazu, N., Taguchi, Y., Hirayama, T., Sasaki, A., Hirabayashi, T., Koide, T., Kitsukawa, T.,
866   Hamada, S., and Yagi, T. (2005). Monoallelic yet combinatorial expression of variable exons of the
867   protocadherin-alpha gene cluster in single neurons. Nature Genetics *37*, 171-176.

868   Evans, P.R., and Murshudov, G.N. (2013). How good are my data and what is the resolution? Acta
869   Crystallographica Section D: Biological Crystallography *69*, 1204-1214.

870   Fan, L., Lu, Y., Shen, X., Shao, H., Suo, L., and Wu, Q. (2018). Alpha protocadherins and Pyk2 kinase
871   regulate cortical neuron migration and cytoskeletal dynamics via Rac1 GTPase and WAVE complex in
872   mice. eLife *7*, e35242.

873   Fukuda, E., Hamada, S., Hasegawa, S., Katori, S., Sanbo, M., Miyakawa, T., Yamamoto, T., Yamamoto,
874   H., Hirabayashi, T., and Yagi, T. (2008). Down-regulation of protocadherin-α A isoforms in mice changes
875   contextual fear conditioning and spatial working memory. European Journal of Neuroscience *28*, 1362-
876   1376.

877   Garrett, A.M., Bosch, P.J., Steffen, D.M., Fuller, L.C., Marcucci, C.G., Koch, A.A., Bais, P., Weiner, J.A.,
878   and Burgess, R.W. (2019). CRISPR/Cas9 interrogation of the mouse Pcdhg gene cluster reveals a crucial
879   isoform-specific role for Pcdhgc4. PLOS Genetics *15*, e1008554.

880   Goodman, K.M., Rubinstein, R., Dan, H., Bahna, F., Mannepalli, S., Ahlsén, G., Aye Thu, C., Sampogna,
881   R.V., Maniatis, T., Honig, B.*, et al.* (2017). Protocadherin *cis*-dimer architecture and recognition unit
882   diversity. Proceedings of the National Academy of Sciences *114*, E9829-E9837.

883   Goodman, K.M., Rubinstein, R., Thu, C.A., Bahna, F., Mannepalli, S., Ahlsen, G., Rittenhouse, C.,
884   Maniatis, T., Honig, B., and Shapiro, L. (2016a). Structural Basis of Diverse Homophilic Recognition by
885   Clustered alpha- and beta-Protocadherins. Neuron *90*, 709-723.

886   Goodman, K.M., Rubinstein, R., Thu, C.A., Mannepalli, S., Bahna, F., Ahlsén, G., Rittenhouse, C.,
887   Maniatis, T., Honig, B., and Shapiro, L. (2016b). γ-Protocadherin structural diversity and functional
888   implications. eLife *5*, e20930.

889   Goodman, K.M., Yamagata, M., Jin, X., Mannepalli, S., Katsamba, P.S., Ahlsén, G., Sergeeva, A.P., Honig,
890   B., Sanes, J.R., and Shapiro, L. (2016c). Molecular basis of sidekick-mediated cell-cell adhesion and
891   specificity. eLife *5*, e19058.

892   Harrison, O.J., Brasch, J., Katsamba, P.S., Ahlsen, G., Noble, A.J., Dan, H., Sampogna, R.V., Potter, C.S.,
893   Carragher, B., Honig, B.*, et al.* (2020). Family-wide Structural and Biophysical Analysis of Binding
894   Interactions among Non-clustered δ-Protocadherins. Cell Reports *30*, 2655-2671.e2657.

895   Harrison, O.J., Vendome, J., Brasch, J., Jin, X., Hong, S., Katsamba, P.S., Ahlsen, G., Troyanovsky, R.B.,
896   Troyanovsky, S.M., Honig, B.*, et al.* (2012). Nectin ectodomain structures reveal a canonical adhesive
897   interface. Nature Structural & Molecular Biology *19*, 906-915.

898   Hasegawa, S., Kumagai, M., Hagihara, M., Nishimaru, H., Hirano, K., Kaneko, R., Okayama, A.,
899   Hirayama, T., Sanbo, M., and Hirabayashi, M. (2016). Distinct and Cooperative Functions for the

900 Protocadherin-α,-β and-γ Clusters in Neuronal Survival and Axon Targeting. Frontiers in Molecular
901 Neuroscience *9*, 155.

902 Hattori, D., Chen, Y., Matthews, B.J., Salwinski, L., Sabatti, C., Grueber, W.B., and Zipursky, S.L. (2009).
903 Robust discrimination between self and non-self neurites requires thousands of Dscam1 isoforms. Nature
904 *461*, 644-U687.

905 Honig, B., and Shapiro, L. (2020). Adhesion Protein Structure, Molecular Affinities, and Principles of Cell-
906 Cell Recognition. Cell *181*, 520-535.

907 Hudson, J.D., Tamilselvan, E., Sotomayor, M., and Cooper, S.R. (2021). A complete Protocadherin-19
908 ectodomain model for evaluating epilepsy-causing mutations and potential protein interaction sites.
909 Structure.

910 Ing-Esteves, S., Kostadinov, D., Marocha, J., Sing, A.D., Joseph, K.S., Laboulaye, M.A., Sanes, J.R., and
911 Lefebvre, J.L. (2018). Combinatorial Effects of Alpha- and Gamma-Protocadherins on Neuronal Survival
912 and Dendritic Self-Avoidance. The Journal of Neuroscience *38*, 2713-2729.

913 Iqbal, M., Maroofian, R., Çavdarlı, B., Riccardi, F., Field, M., Banka, S., Bubshait, D.K., Li, Y., Hertecant,
914 J., Baig, S.M.*, et al.* (2021). Biallelic variants in PCDHGC4 cause a novel neurodevelopmental syndrome
915 with progressive microcephaly, seizures, and joint anomalies. Genetics in Medicine.

916 Kabsch, W. (2010). XDS. Acta Crystallographica Section D: Biological Crystallography *66*, 125-132.

917 Kaneko, R., Kato, H., Kawamura, Y., Esumi, S., Hirayama, T., Hirabayashi, T., and Yagi, T. (2006). Allelic
918 gene regulation of Pcdh-alpha and Pcdh-gamma clusters involving both monoallelic and biallelic
919 expression in single Purkinje cells. Journal of Biological Chemistry *281*, 30551-30560.

920 Katsamba, P., Carroll, K., Ahlsen, G., Bahna, F., Vendome, J., Posy, S., Rajebhosale, M., Price, S., Jessell,
921 T.M., Ben-Shaul, A.*, et al.* (2009). Linking molecular affinity and cellular specificity in cadherin-mediated
922 adhesion. Proceedings of the National Academy of Sciences *106*, 11594-11599.

923 Keeler, A.B., Schreiner, D., and Weiner, J.A. (2015). Protein Kinase C Phosphorylation of a γ-
924 Protocadherin C-terminal Lipid Binding Domain Regulates Focal Adhesion Kinase Inhibition and Dendrite
925 Arborization. Journal of Biological Chemistry *290*, 20674-20686.

926 Kostadinov, D., and Sanes, J.R. (2015). Protocadherin-dependent dendritic self-avoidance regulates neural
927 connectivity and circuit function. Elife *4*.

928 Krissinel, E., and Henrick, K. (2007). Inference of Macromolecular Assemblies from Crystalline State.
929 Journal of Molecular Biology *372*, 774-797.

930 Lefebvre, J.L., Kostadinov, D., Chen, W.V., Maniatis, T., and Sanes, J.R. (2012). Protocadherins mediate
931 dendritic self-avoidance in the mammalian nervous system. Nature *488*, 517-521.

932   Liebschner, D., Afonine, P.V., Baker, M.L., Bunkoczi, G., Chen, V.B., Croll, T.I., Hintze, B., Hung, L.-
933   W., Jain, S., McCoy, A.J., *et al.* (2019). Macromolecular structure determination using X-rays, neutrons
934   and electrons: recent developments in Phenix. Acta Crystallographica Section D *75*, 861-877.

935   Mah, K.M., Houston, D.W., and Weiner, J.A. (2016). The gamma-Protocadherin-C3 isoform inhibits
936   canonical Wnt signalling by binding to and stabilizing Axin1 at the membrane. Scientific Reports *6*.

937   Mah, K.M., and Weiner, J.A. (2017). Regulation of Wnt signaling by protocadherins. Seminars in Cell &
938   Developmental Biology *69*, 158-171.

939   McCoy, A.J., Grosse-Kunstleve, R.W., Adams, P.D., Winn, M.D., Storoni, L.C., and Read, R.J. (2007).
940   Phaser crystallographic software. Journal of Applied Crystallography *40*, 658-674.

941   Miura, S.K., Martins, A., Zhang, K.X., Graveley, B.R., and Zipursky, S.L. (2013). Probabilistic Splicing of
942   Dscam1 Establishes Identity at the Level of Single Neurons. Cell *155*, 1166-1177.

943   Modak, D., and Sotomayor, M. (2019). Identification of an adhesive interface for the non-clustered δ1
944   protocadherin-1 involved in respiratory diseases. Communications Biology *2*, 354.

945   Molumby, M.J., Anderson, R.M., Newbold, D.J., Koblesky, N.K., Garrett, A.M., Schreiner, D., Radley,
946   J.J., and Weiner, J.A. (2017). γ-Protocadherins Interact with Neuroligin-1 and Negatively Regulate
947   Dendritic Spine Morphogenesis. Cell Reports *18*, 2702-2714.

948   Mountoufaris, G., Canzio, D., Nwakeze, C.L., Chen, W.V., and Maniatis, T. (2016). Writing, Reading, and
949   Translating the Clustered Protocadherin Cell Surface Recognition Code for Neural Circuit Assembly.
950   Annual Review of Cell and Developmental Biology *34*, 471-493.

951   Mountoufaris, G., Chen, W.V., Hirabayashi, Y., O'Keeffe, S., Chevee, M., Nwakeze, C.L., Polleux, F., and
952   Maniatis, T. (2017). Multicluster Pcdh diversity is required for mouse olfactory neural circuit assembly.
953   Science *356*, 411-414.

954   Murata, Y., Hamada, S., Morishita, H., Mutoh, T., and Yagi, T. (2004). Interaction with Protocadherin-γ
955   Regulates the Cell Surface Expression of Protocadherin-α. Journal of Biological Chemistry *279*, 49508-
956   49516.

957   Nicoludis, J.M., Green, A.G., Walujkar, S., May, E.J., Sotomayor, M., Marks, D.S., and Gaudet, R. (2019).
958   Interaction specificity of clustered protocadherins inferred from sequence covariation and structural
959   analysis. Proceedings of the National Academy of Sciences *116*, 17825-17830.

960   Nicoludis, J.M., Lau, S.-Y., Schaerfe, C.P.I., Marks, D.S., Weihofen, W.A., and Gaudet, R. (2015).
961   Structure and Sequence Analyses of Clustered Protocadherins Reveal Antiparallel Interactions that Mediate
962   Homophilic Specificity. Structure *23*, 2087-2098.

963   Nicoludis, J.M., Vogt, B.E., Green, A.G., Scharfe, C.P.I., Marks, D.S., and Gaudet, R. (2016). Antiparallel
964   protocadherin homodimers use distinct affinity- and specificity-mediating regions in cadherin repeats 1-4.
965   eLife *5*.

966   Onouchi, T., Kishino-Kaneko, Y., Kameshita, I., Ishida, A., and Sueyoshi, N. (2015). Regulation of
967   Ca2+/calmodulin-dependent protein kinase phosphatase (CaMKP/PPM1F) by protocadherin-γC5 (Pcdh-
968   γC5). Archives of Biochemistry and Biophysics *585*, 109-120.

969   Pancho, A., Aerts, T., Mitsogiannis, M.D., and Seuntjens, E. (2020). Protocadherins at the Crossroad of
970   Signaling Pathways. Front Mol Neurosci *13*, 117.

971   Peek, S.L., Mah, K.M., and Weiner, J.A. (2017). Regulation of neural circuit formation by protocadherins.
972   Cellular and Molecular Life Sciences.

973   Petersen, T.N., Brunak, S., von Heijne, G., and Nielsen, H. (2011). SignalP 4.0: discriminating signal
974   peptides from transmembrane regions. Nat Meth *8*, 785-786.

975   Pettersen, E.F., Goddard, T.D., Huang, C.C., Couch, G.S., Greenblatt, D.M., Meng, E.C., and Ferrin, T.E.
976   (2004). UCSF Chimera—A visualization system for exploratory research and analysis. Journal of
977   Computational Chemistry 25, 1605-1612.

978   Phillips, G.R., LaMassa, N., and Nie, Y.M. (2017). Clustered protocadherin trafficking. Seminars in Cell
979   & Developmental Biology *69*, 131-139.

980   Rich, R.L., and Myszka, D.G. (2007). Survey of the year 2006 commercial optical biosensor literature.
981   Journal of Molecular Recognition *20*, 300-366.

982   Robert, X., and Gouet, P. (2014). Deciphering key features in protein structures with the new ENDscript
983   server. Nucleic Acids Research *42*, W320-W324.

984   Rubinstein, R., Goodman, K.M., Maniatis, T., Shapiro, L., and Honig, B. (2017). Structural origins of
985   clustered protocadherin-mediated neuronal barcoding. Seminars in Cell & Developmental Biology *69*, 140-
986   150.

987   Rubinstein, R., Thu, C.A., Goodman, K.M., Wolcott, H.N., Bahna, F., Mannepalli, S., Ahlsen, G., Chevee,
988   M., Halim, A., Clausen, H.*, et al.* (2015). Molecular Logic of Neuronal Self-Recognition through
989   Protocadherin Domain Interactions. Cell *163*, 629-642.

990   Schmucker, D., Clemens, J.C., Shu, H., Worby, C.A., Xiao, J., Muda, M., Dixon, J.E., and Zipursky, S.L.
991   (2000). Drosophila Dscam is an axon guidance receptor exhibiting extraordinary molecular diversity. Cell
992   *101*, 671-684.

993   Schreiner, D., and Weiner, J.A. (2010). Combinatorial homophilic interaction between gamma-
994   protocadherin multimers greatly expands the molecular diversity of cell adhesion. Proceedings of the
995   National Academy of Sciences of the United States of America *107*, 14893-14898.

996   Sergeeva, A.P., Katsamba, P.S., Cosmanescu, F., Brewer, J.J., Ahlsen, G., Mannepalli, S., Shapiro, L., and
997   Honig, B. (2020). DIP/Dpr interactions and the evolutionary design of specificity in protein families. Nat
998   Commun *11*, 2125.

36

999   Shapovalov, M.V., and Dunbrack, R.L., Jr. (2011). A smoothed backbone-dependent rotamer library for
1000 proteins derived from adaptive kernel density estimates and regressions. Structure *19*, 844-858.

1001 Sievers, F., Wilm, A., Dineen, D., Gibson, T.J., Karplus, K., Li, W., Lopez, R., McWilliam, H., Remmert,
1002 M., Söding, J*., et al.* (2011). Fast, scalable generation of high-quality protein multiple sequence alignments
1003 using Clustal Omega. Molecular Systems Biology *7*, 539-539.

1004 Steffen, D.M., Ferri, S.L., Marcucci, C.G., Blocklinger, K.L., Molumby, M.J., Abel, T., and Weiner, J.A.
1005 (2021). The γ-Protocadherins Interact Physically and Functionally with Neuroligin-2 to Negatively
1006 Regulate Inhibitory Synapse Density and Are Required for Normal Social Interaction. Molecular
1007 Neurobiology *58*, 2574-2589.

1008 Strong, M., Sawaya, M.R., Wang, S., Phillips, M., Cascio, D., and Eisenberg, D. (2006). Toward the
1009 structural genomics of complexes: Crystal structure of a PE/PPE protein complex from Mycobacterium
1010 tuberculosis. Proceedings of the National Academy of Sciences of the United States of America *103*, 8060-
1011 8065.

1012 Thu, C.A., Chen, W.V., Rubinstein, R., Chevee, M., Wolcott, H.N., Felsovalyi, K.O., Tapia, J.C., Shapiro,
1013 L., Honig, B., and Maniatis, T. (2014). Single-Cell Identity Generated by Combinatorial Homophilic
1014 Interactions between alpha, beta, and gamma Protocadherins. Cell *158*, 1045-1059.

1015 Vendome, J., Felsovalyi, K., Song, H., Yang, Z., Jin, X., Brasch, J., Harrison, O.J., Ahlsen, G., Bahna, F.,
1016 Kaczynska, A*., et al.* (2014). Structural and energetic determinants of adhesive binding specificity in type
1017 I cadherins. Proceedings of the National Academy of Sciences of the United States of America *111*, E4175-
1018 E4184.

1019 Winn, M.D., Ballard, C.C., Cowtan, K.D., Dodson, E.J., Emsley, P., Evans, P.R., Keegan, R.M., Krissinel,
1020 E.B., Leslie, A.G.W., McCoy, A*., et al.* (2011). Overview of the CCP4 suite and current developments.
1021 Acta Crystallographica Section D *67*, 235-242.

1022 Wojtowicz, W.M., Flanagan, J.J., Millard, S.S., and Zipursky, S.L. (2004). Alternative splicing of
1023 Drosophila Dscam generates axon guidance receptors that exhibit isoform-specific homophilic binding.
1024 Cell *118*, 619-633.

1025 Wojtowicz, W.M., Wu, W., Andre, I., Qian, B., Baker, D., and Zipursky, S.L. (2007). A vast repertoire of
1026 Dscam binding Specificities arises from modular interactions of variable ig domains. Cell *130*, 1134-1145.

1027 Wu, Q., and Maniatis, T. (1999). A striking organization of a large family of human neural cadherin-like
1028 cell adhesion genes. Cell *97*, 779-790.

1029 Wu, Q., Zhang, T., Cheng, J.F., Kim, Y., Grimwood, J., Schmutz, J., Dickson, M., Noonan, J.P., Zhang,
1030 M.Q., Myers, R.M*., et al.* (2001). Comparative DNA sequence analysis of mouse and human protocadherin
1031 gene clusters. Genome Research *11*, 389-404.

1032 Wu, W., Ahlsen, G., Baker, D., Shapiro, L., and Zipursky, S.L. (2012). Complementary Chimeric Isoforms
1033 Reveal Dscam1 Binding Specificity In Vivo. Neuron *74*, 261-268.

1034   Wu, Y., Honig, B., and Ben-Shaul, A. (2013). Theory and Simulations of Adhesion Receptor Dimerization
1035   on Membrane Surfaces. Biophysical Journal *104*, 1221-1229.

1036   Zipursky, S.L., and Grueber, W.B. (2013). The Molecular Basis of Self-Avoidance. In Annual Review of
1037   Neuroscience, Vol 36, S.E. Hyman, ed., pp. 547-568.

1038

1039

Figure 1
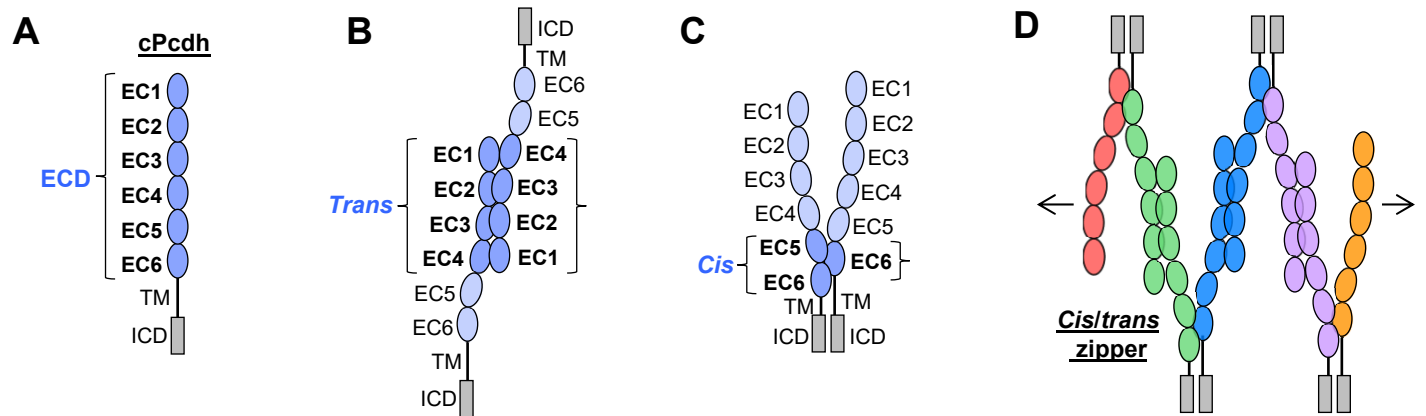
Figure 1: cPcdh domain organization and extracellular interactions

(A) Schematic depicting the domain organization of cPcdhs. EC, extracellular cadherin domain; TM, transmembrane domain; ECD, ectodomain; ICD, intracellular domain.

(B) Schematic of two cPcdhs interacting via the EC1–4 *trans* interface.

(C) Schematic of two cPcdhs interacting via the EC5–6/EC6 *cis* interface.

(D) Schematic depiction of the *cis/trans* cPcdh zipper comprising multiple cPcdh isoforms (various colors) engaged in homophilic *trans* interactions and promiscuous *cis* interactions as required for the proposed "isoform-mismatch chain-termination model" of cPcdh-mediated neuronal self-recognition and self-avoidance.
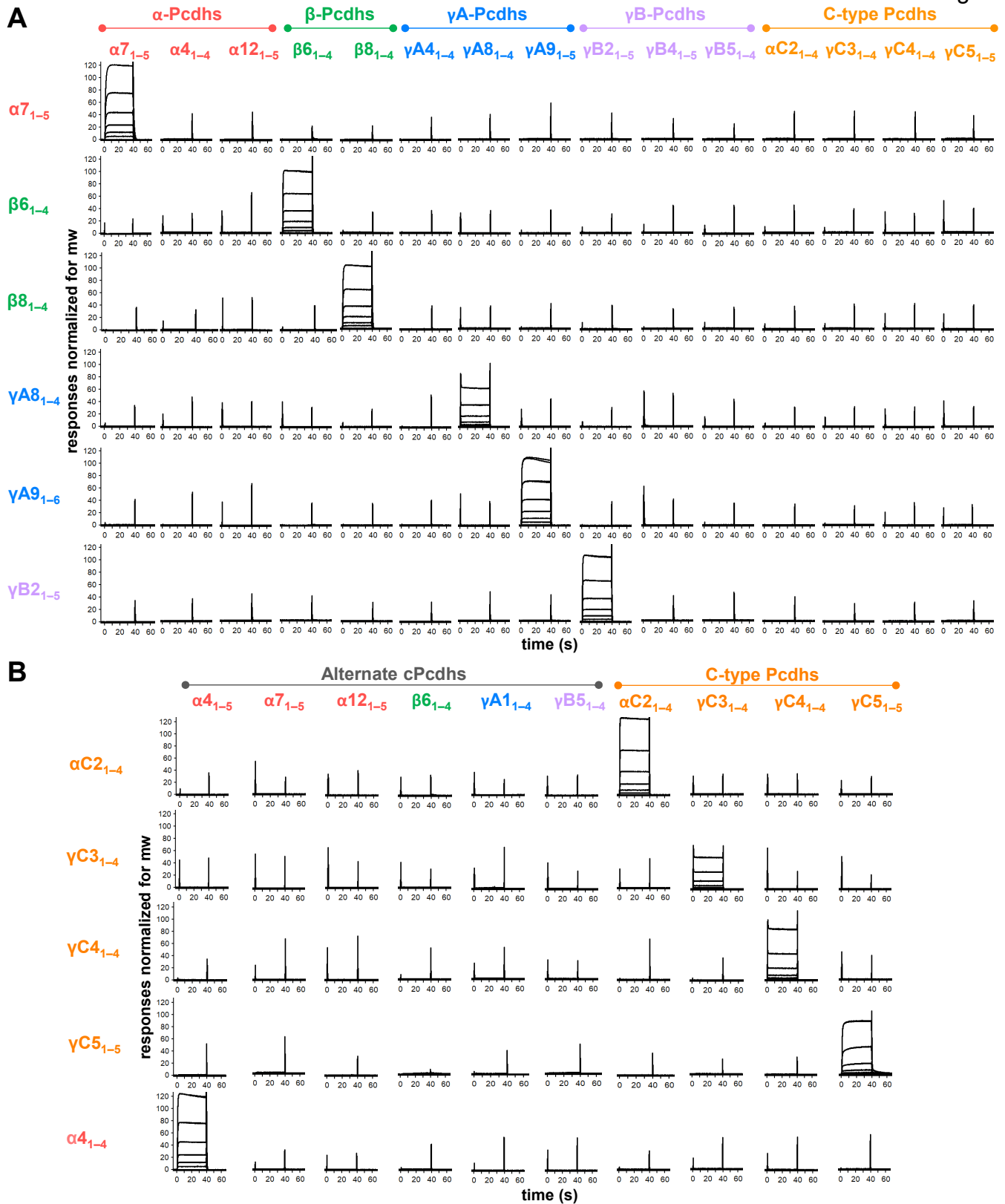
Figure 2: cPcdhs show strict homophilic specificity in their *trans* interactions
(A) SPR binding profiles of cPcdh *trans* fragment analytes from all cPcdh subfamilies (denoted in the top row) flowed over six surfaces coated with alternate cPcdh *trans* fragments (rows). Responses over all surfaces are drawn on the same scale and normalized for molecular weight.
**(B)** SPR binding profiles of cPcdh *trans* fragment analytes from all cPcdh subfamilies (shown in columns) flowed over individual surfaces coated with C-type and α4 cPcdh *trans* fragments (rows). Responses over all surfaces are drawn on the same scale and normalized for molecular weight.

Figure 3

A

$\gamma C4_{1-4}$ *trans* dimer crystal structures

Crystal form 1
PDB 7JGZ

Crystal form 2
PDB 7RGF

Superposition

RMSD, 2.98 Å over 750 Cαs

B

Interfacial differences between the $\gamma C4_{1-4}$ structures

Crystal form 1
BSA = 3800 Å^2
(intact interface)

Crystal form 2
BSA = 2900 Å^2
(disrupted EC2:EC3 interface)

C

Comparison between specific regions of the $\gamma C4$ and $\gamma B2$ *trans* dimer interfaces

EC1:EC4

EC2:EC3

D

Protein	Oligomeric State	Dissociation Constant, K_D (µM)
$\gamma C4_{1-4}$ wt	Monomer / Very weak dimer	> 500
$\gamma C4_{1-4}$ E78A	Dimer	58 ± 0.60
$\gamma C4_{1-4}$ E78Q	Dimer	83 ± 2.6
$\gamma C4_{1-4}$ S344R	Dimer	112 ± 14
$\gamma C4_{1-4}$ D290A	Monomer	N/A
$\gamma C4_{1-4}$ D290N	Monomer	N/A

Figure 3: C-type cPcdh γC4 adopts an EC1–4-mediated head-to-tail *trans* dimer like alternate cPcdhs with a comparatively weak dimer affinity

(A) Ribbon diagrams of the $\gamma C4_{EC1-4}$ *trans* dimer crystal structures obtained from two different crystal forms. Bound calcium ions are shown as green spheres and glycans are shown in pale blue spheres.

(B) The two crystal structures have a markedly different *trans* interface buried surface area (BSA). *Left,* Surface views of the two *trans* dimer crystal structures highlight the difference, with a gap apparent in the EC2:EC3 region of the interface in crystal form 2 that is absent from crystal form 1. Surfaces are colored by atom type with the carbons colored orange for crystal form 1 and yellow for crystal form 2. *Right,* Close up view of the gap region in the crystal form 2 dimer with the side chains depicted as sticks. The intact crystal form 1 γC4 dimer is similar overall to those of the published intact alternate α, β, γA, and γB cPcdhs and the published δ2 non-clustered (nc) Pcdh *trans* dimers (root mean square deviation over aligned Cαs (RMSD) 2.4–4.5 Å; Figure 3—source data 2). The published crystal structures of γA8, γA1, and γB3 also show partially disrupted *trans* interfaces though in differing regions of the interface (Goodman et al., 2016b, Nicoludis et al., 2016).

(C) Comparison between the (i) EC1:EC4 and (ii) EC2:EC3 regions of the γC4 (orange) and γB2 (blue, PDB 5T9T) *trans* dimer interfaces. (i) Structural alignment of the EC1:EC4 portion of the γC4 and γB2 *trans* dimers highlights a possible destabilizing role for γC4 residue E78 since unlike its counterpart in γB2 (D77) it is not juxtaposed with a basic residue. (ii) Similarly, an additional negatively charged residue (D290) which occupies a central position in the γC4 EC2:EC3 interface may also contribute to γC4's comparatively weak *trans* dimer interaction. Distances between the D290 side chain and its nearest contacts are shown as dashed grey lines with distances given in Angstroms.

(D) Sedimentation equilibrium AUC experiments were conducted on γC4 EC1–4 wild type (wt) and interface mutants to assess whether E78 and D290 negatively impact *trans* dimerization. Table details the oligomeric state and dissociation constants for each protein tested.

Figure 4

Figure 4: cPcdh *cis* interactions are promiscuous with a preference for interfamily heterodimers
(A) SPR binding profiles of cPcdh *cis* fragment analytes from all cPcdh subfamilies except alphas (shown in columns) flowed over individual surfaces coated with cPcdh *cis* fragments. Binding profiles for each surface are individually scaled and responses are normalized for molecular weight.
(B) Table of dissociation constants calculated from the SPR data for the four monomeric analytes. The number in brackets represents the error of the fit based on analysis of duplicate responses. Binding signals were not detected for interactions labeled NB, while >50, represents interactions with K_Ds >50 µM, where an accurate K_D cannot be determined.
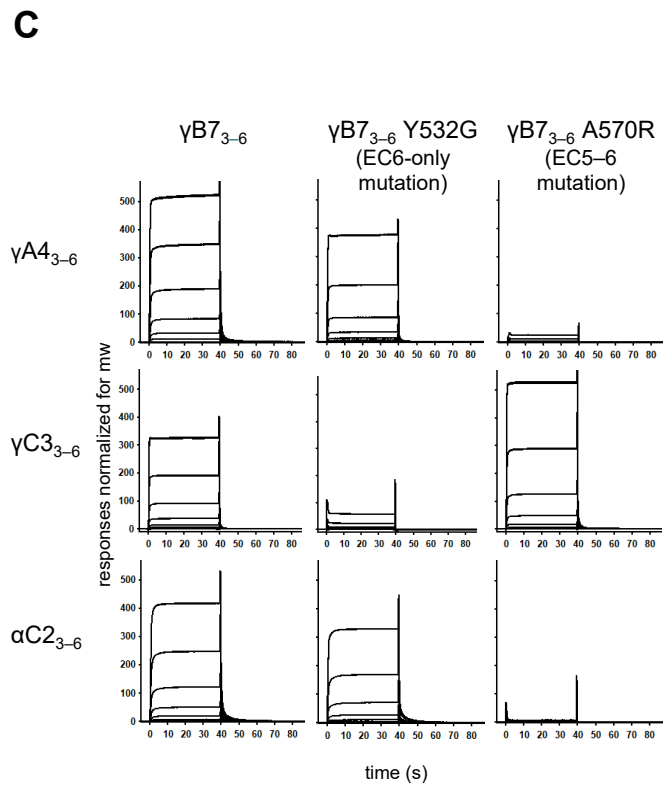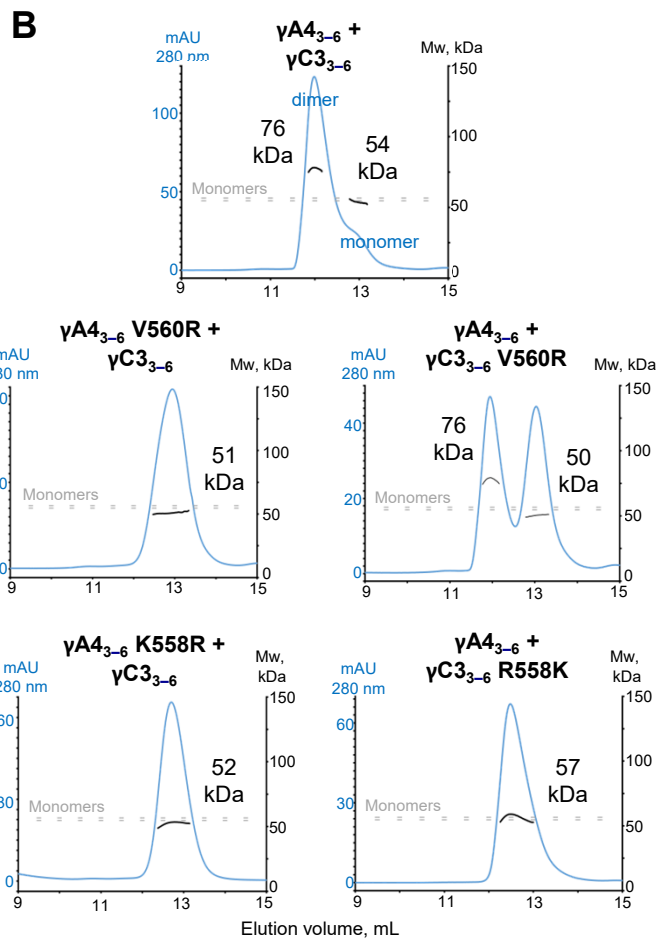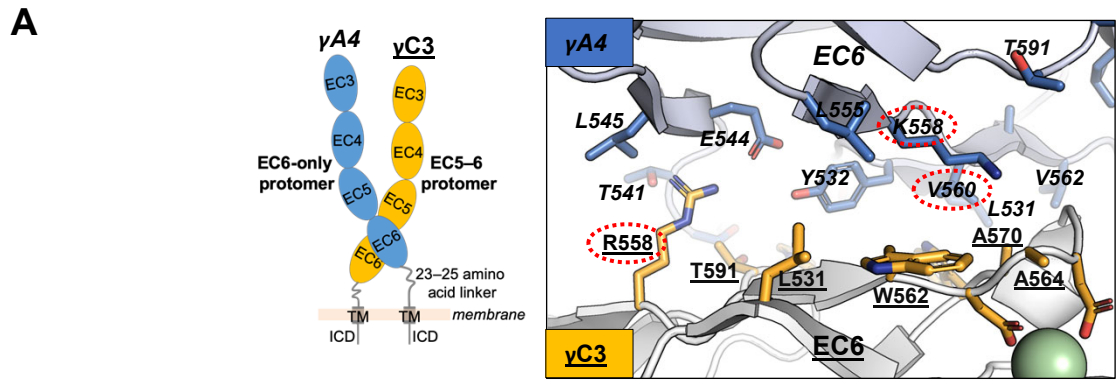
Figure 5: γA4 preferentially forms the EC6-only side and γC3 the EC5–6 side in *cis* dimers

(**A**) Structural model of γA4/γC3 *cis* dimer based on $\gamma B7_{EC3-6}$ *cis* dimer and $\gamma A4_{EC3-6}$ crystal structures (PDBs: 5V5X and 5SZQ). γA4 is shown adopting the EC6-only side (blue protomer) and γC3 is shown adopting the EC5–6 side (yellow protomer). Left, schematic of the γA4/γC3 EC3–6 *cis* dimer. Right, close-up view of the EC6:EC6 interface from the modeled *cis* dimer showing interfacial residue side chains. Bound calcium ions are shown as green spheres. Residues which were mutated in the panel B are circled in red. γB7 crystal structure numbering is used for both γA4 and γC3 residues. See methods for γA4 and γC3 alignment. Please note the model shown here is solely for hypothesis generation, since it is unlikely to be completely accurate. See methods for further details of structural modeling.

(**B**) *Top*, SEC-MALS data for an equimolar mixture of wild-type $\gamma A4_{EC3-6}$ and $\gamma C3_{EC3-6}$ showing dimer formation. Plot shows size exclusion absorbance at 280 nm trace (left axis), molecular weight of the eluant peaks (right axis), and the monomer molecular weights of $\gamma A4_{EC3-6}$ and $\gamma C3_{EC3-6}$ measured by mass spectrometry – 54.5 kDa and 56.5 kDa respectively – as dashed grey lines. Average molecular weight of the molecules in the dimer and monomer eluant peaks are labeled. *Middle*, SEC-MALS data for V560R mutants, which target the EC6-only side of the interface. *Bottom*, SEC-MALS data for residue 558 mutants. The γC3-like K558R mutation in γA4 inhibits heterodimer formation with wild-type γC3. Similarly, the γA4-like R558K in γC3 inhibits dimerization with wild-type γA4.

(**C**) SPR binding profiles for $\gamma B7_{EC3-6}$ wild type and *cis* interface mutants flowed over three individual wild-type *cis* fragment surfaces. The two mutations specifically target one side of the *cis* interface.

Figure 2—figure supplement 1
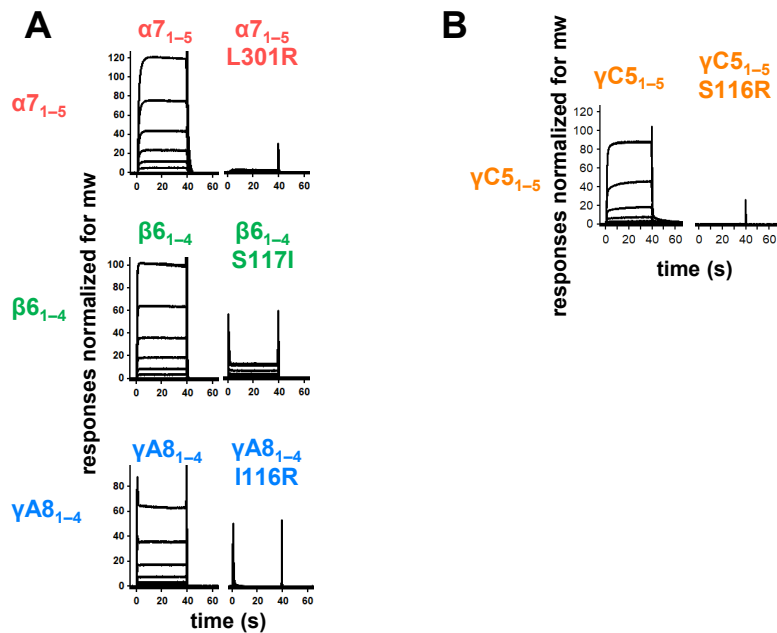
Figure 2—figure supplement 1: *Trans* **interface mutants demonstrate homophilic interactions observed in SPR are mediated by the *trans* dimer interface**

(A) SPR binding curves for wild-type and *trans* mutant alternate cPcdhs flowed over their respective immobilized wild-type molecule.

(B) SPR binding curves for wild-type and *trans* mutant C-type cPcdh γC5 flowed over immobilized wild-type γC5.

Figure 2—figure supplement 2
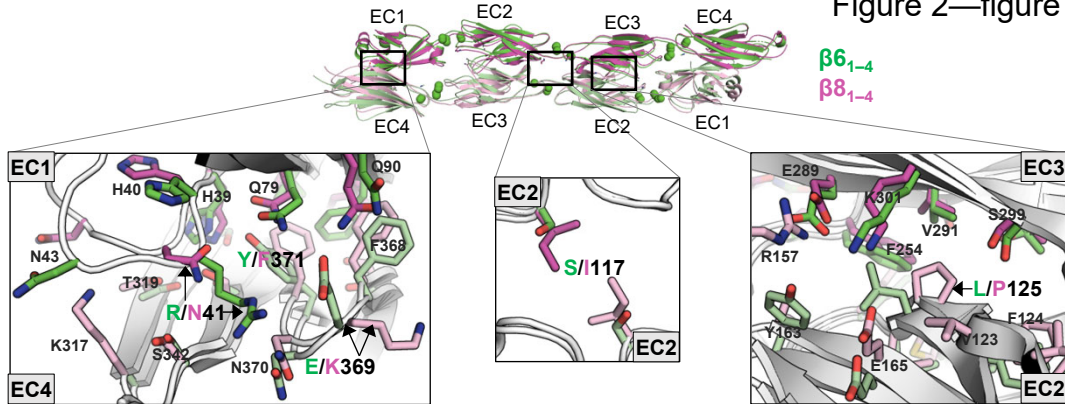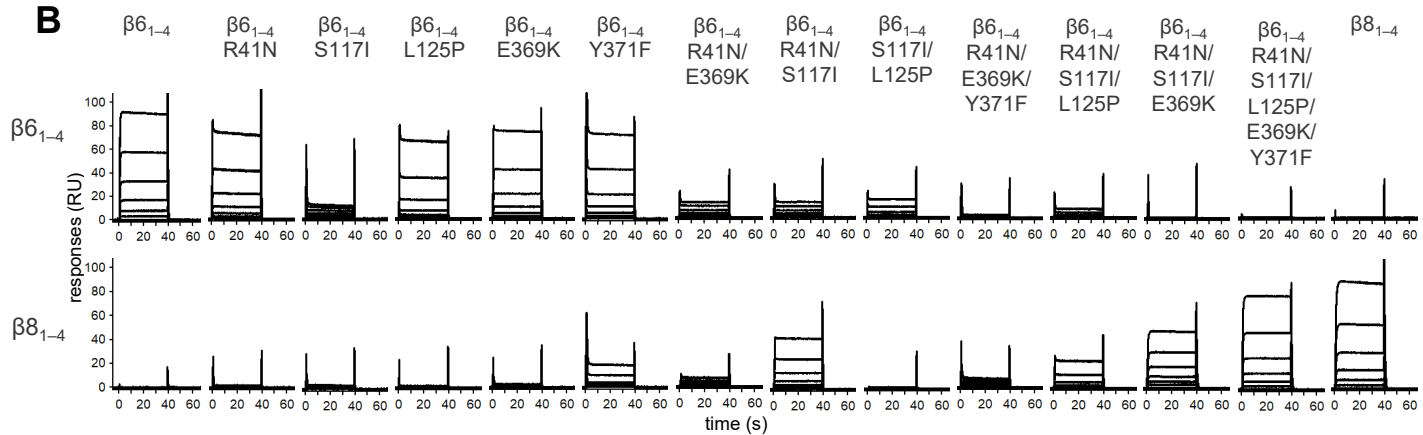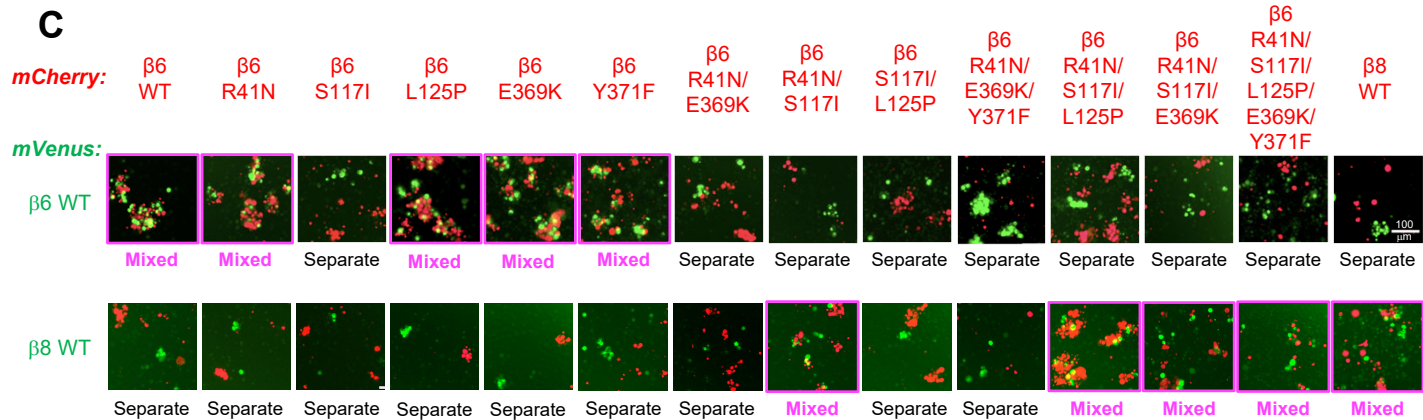
Figure 2 —figure supplement 2: Mutagenesis experiments reveal role in *trans* specificity for the five interfacial residue differences between close pair β6$_{1-4}$ and β8$_{1-4}$

A. Structural superposition of the β6$_{1-4}$ and β8$_{1-4}$ *trans* dimer crystal structures (PDBs: 5DZX and 5DZY) shown in ribbon depiction above, with close-up views of the *trans* interfacial regions containing the five interfacial residues that vary between β6$_{1-4}$ and β8$_{1-4}$ shown below. The two protomers forming the β6$_{1-4}$ dimer are colored green and pale green respectively. The β8$_{1-4}$ dimer is colored magenta/light pink. Bound calcium ions are shown as green spheres. Interfacial residue side chains are shown in the close-up views. The five variable residues are labelled with the β6$_{1-4}$ amino acid given in green and the β8$_{1-4}$ amino acid in magenta: R/N41 is in EC1; E/K369 and Y/F371 are in EC4; S/I117 is in EC2 and self-interacts at the *trans* dimer center of symmetry; and L/P125 is also in EC2.
B. SPR binding profiles of β6 *trans* interface mutants converting β6$_{1-4}$ to β8$_{1-4}$ and the wild-type molecules (shown in columns) were flowed over surfaces coated with wild-type β6$_{1-4}$ or wild-type β8$_{1-4}$ (rows).
C. Results of the K562 co-aggregation assay where cells transfected with mCherry labeled β6 and β8 wild-types (WT) and the same *trans*-specificity mutants as in (**B**) were each mixed with cells transfected with mVenus labeled β6 and β8 wild-types (WT). Experiments where the red and green cells co-aggregate demonstrating interaction between the mCherry-labeled WT or mutant cPcdh and the mVenus-labeled WT cPcdh are labeled "mixed" and highlighted with magenta boxes. Scale bar, 100 μM.

Figure 3—figure supplement 1

A

γC4_{EC1–4} crystal form 1 diffraction anisotropy

(i)

a* direction
b* direction
c* direction
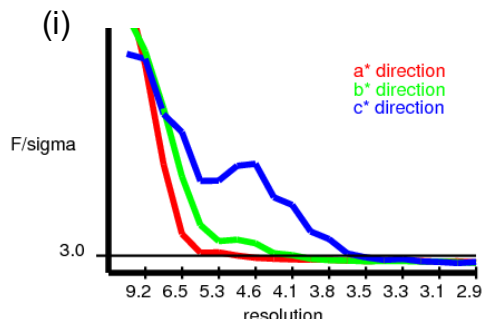
The recommended resolution limits along a*,b*,c* are
4.6 Ang   3.9 Ang   3.5 Ang
These are the resolutions at which F/sigma
drops below an arbitrary cutoff of 3.0

(ii)

B
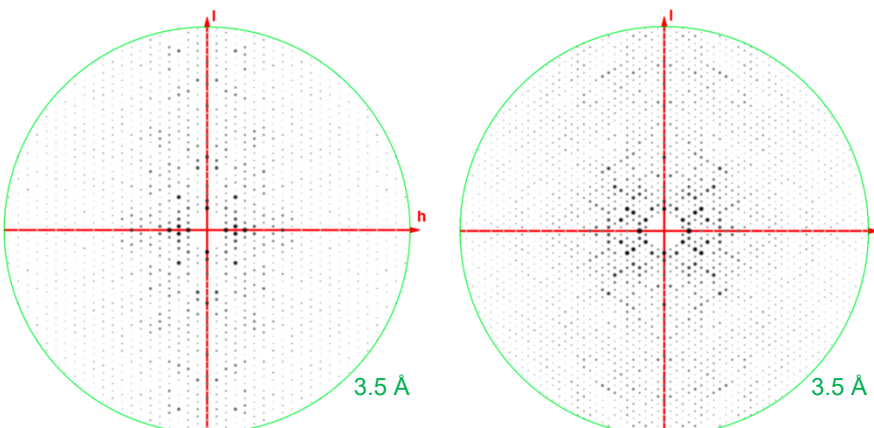
γC4 crystal form 1 *trans* dimer interface

C
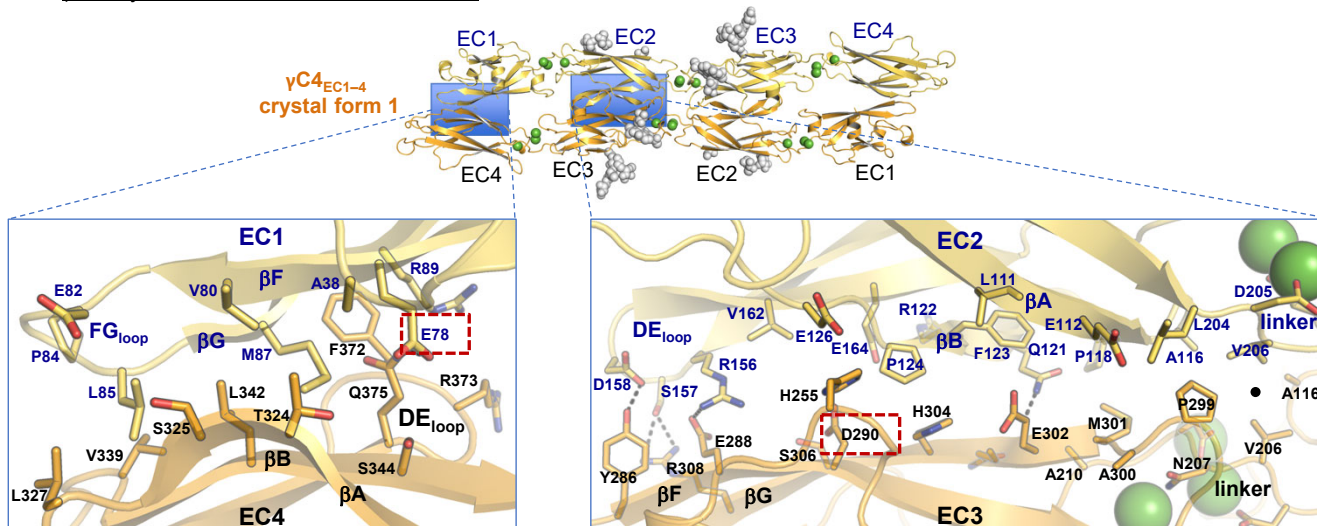
AUC curves for γC4 wild type and *trans* interface mutants
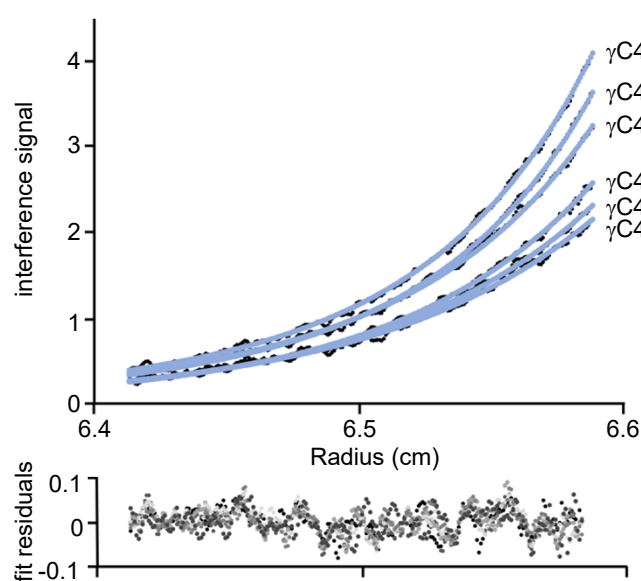
Figure 3—figure supplement 1: γC4 *trans* dimer crystal structures and *trans* interface analysis

(**A**) Our crystallization experiments with γC4_{EC1–4} yielded two distinct crystal forms the first of which showed significant X-ray diffraction anisotropy. (i) UCLA Diffraction Anisotropy Server (Strong et al., 2006) plot shows the F/sigma by resolution along the a*, b* and c* axes. (ii) Synthetic precession photographs of the X-ray diffraction in the k=0 plane (left) and the h=0 plane (right) showing the comparatively stronger/weaker diffraction.

(**B**) Close up views of the EC1:EC4 and EC2:EC3 interfacial regions from the first crystal form. One protomer in the symmetric dimer is colored yellow the other orange. Interfacial residues are labeled, side chains are shown in stick representation and dashed black lines depict potential interfacial hydrogen bond interactions. The two charged residues, E78 and D290, we selected for mutagenesis experiments to see whether they play a destabilizing role in the γC4 *trans* interaction are marked with red dashed boxes.

(**C**) Representative plot of AUC data for the wild type (wt) and mutant γC4 EC1–4 molecules. Raw data are shown in black circles, and the non-linear fits to a monomer-to-dimer model are shown as blue lines. The residuals between the data and fits are shown in the plot below. Table detailing the oligomeric state and dissociation constants determined from the AUC data is shown in Figure 3.

Figure 4—figure supplement 1
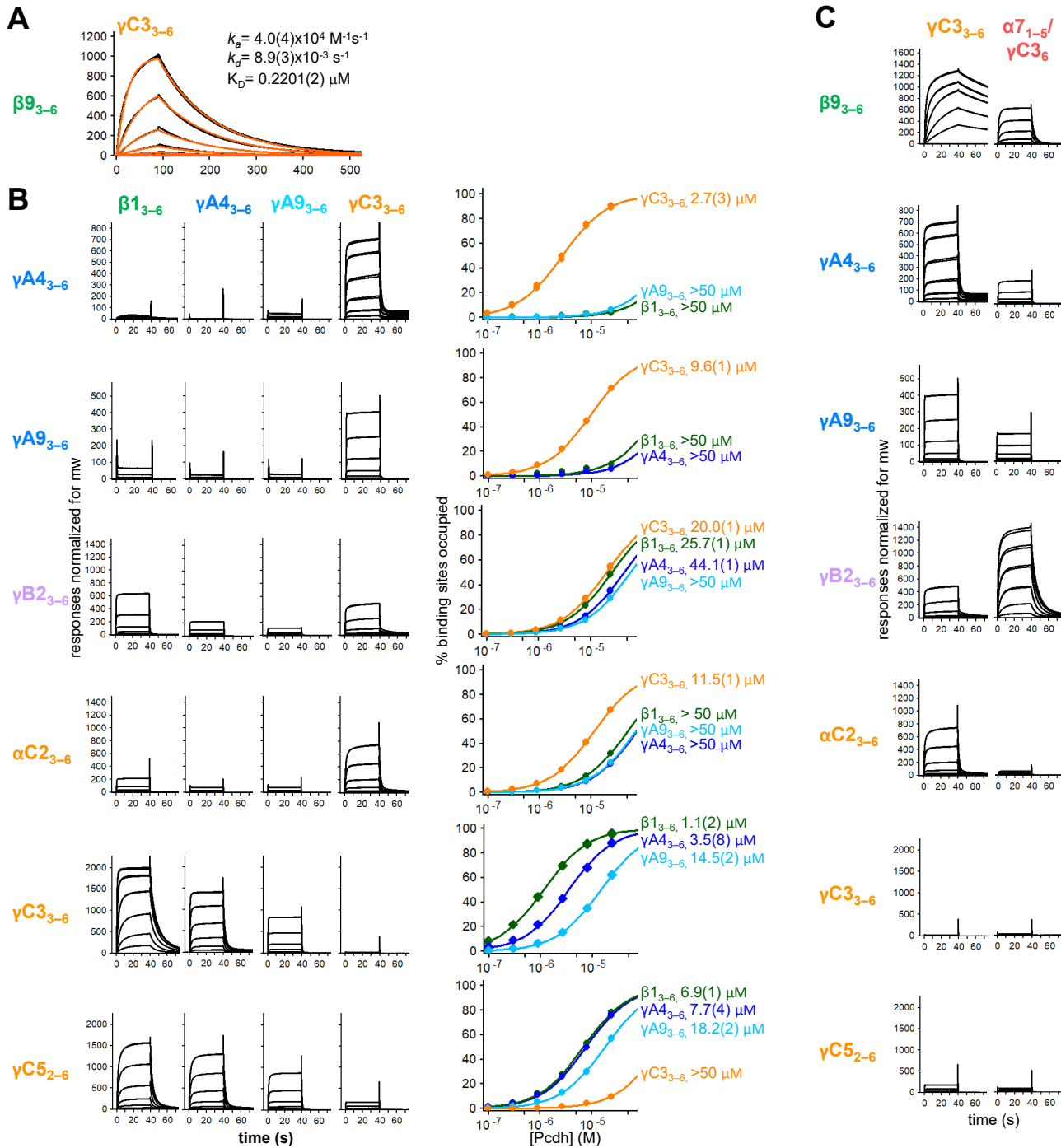
Figure 4—figure supplement 1: Calculation of *cis* interaction dissociation constants and the impact of an α-Pcdh EC5 on family-wide *cis* interactions

(A) Kinetic binding analysis of $\gamma C3_{3-6}$ analyte binding over a $\beta 9_{3-6}$ covered surface. Data is shown in black, and the red traces represent the fit to an 1:1 binding model.

(B) *Left*, SPR binding profiles from Figure 4 for the four monomeric *cis* fragment analytes over all six *cis* fragment surfaces. *Right*, fit of the binding data for these four analytes to 1:1 binding isotherms to calculate K_Ds. $\gamma A4_{3-6}$ and $\gamma A9_{3-6}$ are monomeric and they are not included in the binding isotherms over their respective surface.

(C) SPR binding profiles for $\gamma C3_{3-6}$ (from Figure 4) and an $\alpha 7_{1-5} / \gamma C3_6$ chimera flowed over the immobilized *cis* fragment surfaces. Binding profiles for each surface are individually scaled as in Figure 4.

Figure 4—figure supplement 2
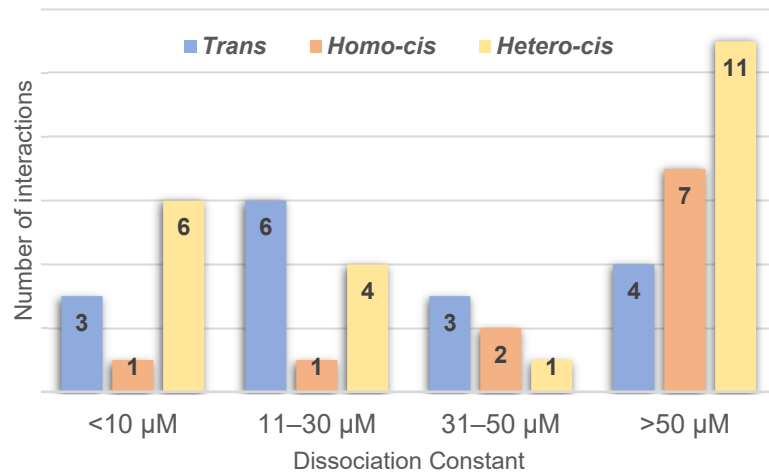
Figure 4—figure supplement 2: Range of cPcdh *cis* and *trans* Dissociation constants, K$_D$s
Chart shows the cPcdh *trans* dimer, homophilic *cis* dimer, and heterophilic *cis* dimer interactions for which we have determined binding affinities divided into four subgroups based on their dissociation constant. The *trans* and homophilic *cis* dimer affinities were determined using AUC (Figure 2—source data 1 and Figure 4—source data 1) and the heterophilic *cis* dimer affinities were determined using SPR (Figure 4B). Of the interactions in the >50 μM group one *trans* interaction and four homophilic *cis* interactions are monomeric in solution (> 500 μM K$_D$ in AUC). Three of the 11 heterophilic *cis* interactions in the >50 μM group show no binding in our SPR experiments based on a 40 RU binding threshold.

Figure 4—figure supplement 3
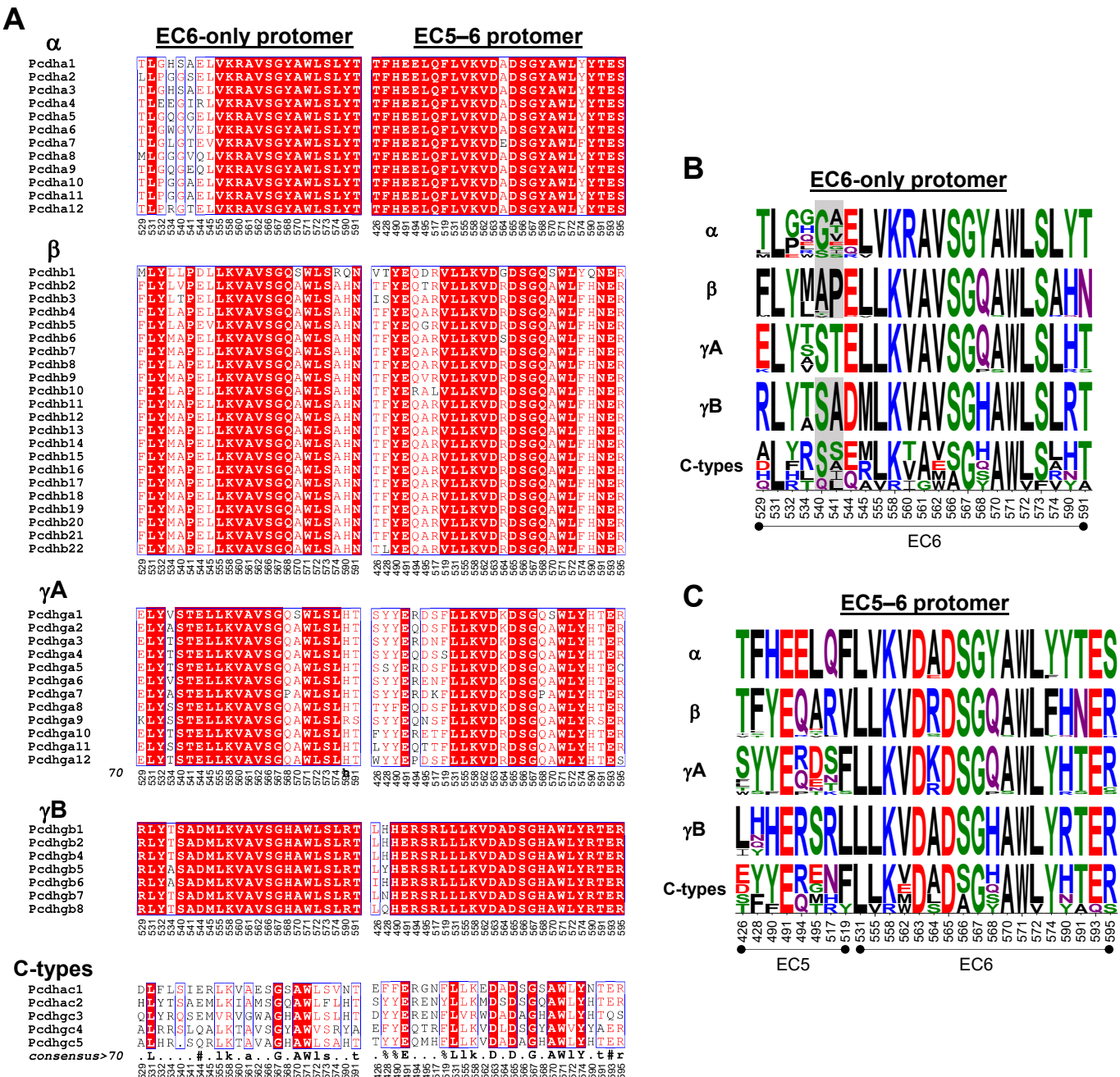
Figure 4—figure supplement 3: Amino acid sequence alignment reveals conservation of *cis* interfacial residues within the alternate cPcdh subfamilies

(A) Amino acid sequence alignments of *cis* interfacial residues from the EC6-only and EC5–6 surfaces for all 58 mouse cPcdhs subdivided by subfamily. Completely conserved residues are highlighted in red with white lettering. Residues 540 and 541 are included in the EC6-only alignments since the crystal structure of γA4 EC3–6 (PDB: 5SZQ) revealed a distinct EC6 A-A'loop architecture to that observed in the γB2, 4, and 7 (PDBs: 5SZR, 6E6B, and 5V5X) *cis* fragment crystal structures that would place these residues in the EC6-only interface if maintained in *cis* interactions.

(B) Sequence logos based on the sequence alignment shown in (**A**) for the EC6-only *cis* interfacial residues from each of the five cPcdh subfamilies highlighting the similarities and conserved differences between the subfamilies. Residues 540 and 541 are included for all isoforms but greyed out for the non-γA isoforms since their involvement may be γA-specific. NB: Previous studies have shown that α-Pcdhs have an impaired EC6-only interface (Thu et al., 2014; Goodman et al., 2017).

(C) Sequence logos for the EC5–6 *cis* interfacial residues from each of the five cPcdh subfamilies

Figure 5—figure supplement 1
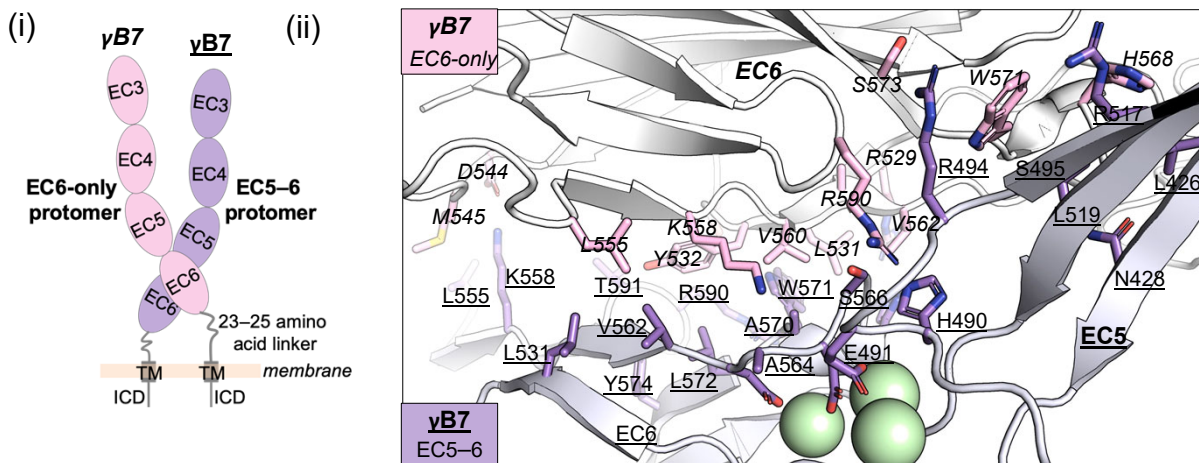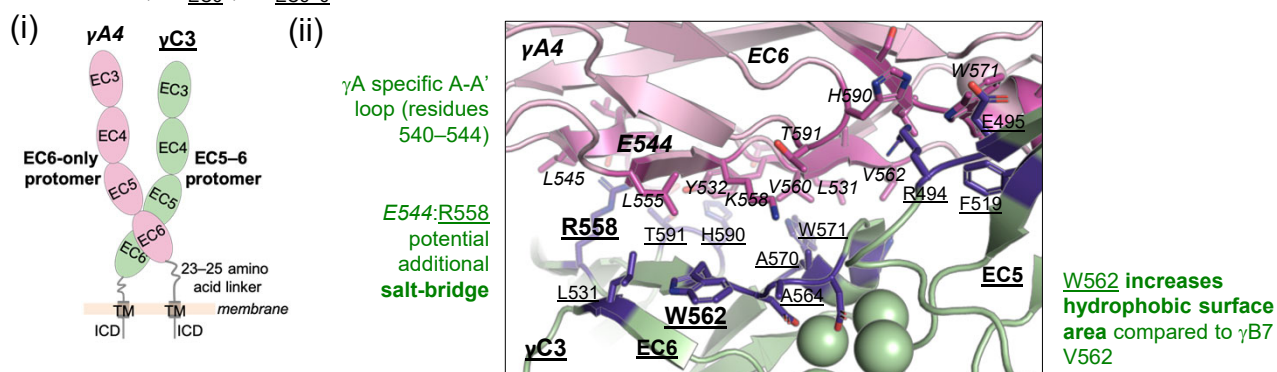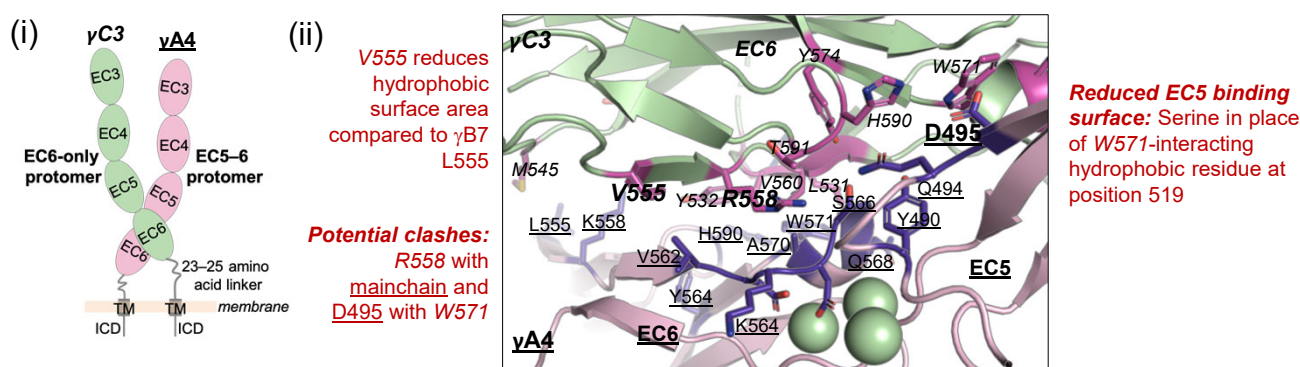
Figure 5—figure supplement 1: Structure-guided sequence analysis of γA4 and γC3 *cis* interactions

(**A**) (i) Schematic of the asymmetric γB7$_{EC3-6}$ *cis* dimer crystal structure. (ii) Close-up view of the γB7 *cis* interface: Interfacial residue side chains are shown in pink for the EC6-only protomer and purple for the EC5–6 protomer. Bound calcium ions are shown as green spheres.

(**B**) (i) Schematic of the γA4$_{EC6}$/γC3$_{EC5-6}$ *cis* dimer. (ii) Model of the γA4$_{EC6}$/γC3$_{EC5-6}$ *cis* dimer interaction generated using structural alignment of EC6 from the monomeric γA4 EC3–6 crystal structure (PDB 5SZQ) to the γB7 EC3–6 *cis* dimer structure for the EC6-only side and computational mutagenesis of γB7 to γC3 selecting the best-fit rotamer (without energy minimization) for the EC5–6 side. The model suggests that this will be the preferred orientation for the γA4/γC3 *cis* dimer interaction. Favorable residue differences between γB7 from (A) and γA4/γC3 in this orientation are noted in green. Please note the model shown here is only used for hypothesis generation, since it is unlikely to be completely accurate.

(**C**) (i) Schematic of the γC3$_{EC6}$/γA4$_{EC5-6}$ *cis* dimer. (ii) Model of the γC3$_{EC6}$/γA4$_{EC5-6}$ *cis* dimer generated using computational mutagenesis of γB7 to γC3 selecting the best-fit rotamer (without energy minimization) for the EC6-only side and structural alignment of EC5–6 from the γA4 EC3–6 crystal structure to the γB7 EC3–6 *cis* dimer structure for the EC5–6 side. The model suggests that this orientation for the γA4/γC3 *cis* dimer interaction will be disfavored. Unfavorable residue differences between γB7 and γA4/γC3 in this orientation are noted in red. Please note the model shown here is unlikely to be completely accurate and is simply for hypothesis generation.

Figure 5—figure supplement 2

A

γA4$_{3-6}$

mAU
280 nm

Mw, kDa

Monomer
54.5 kDa

50
kDa

γC3$_{3-6}$

mAU
280 nm

Mw, kDa

Monomer
56.5 kDa

52
kDa

γC3$_{3-6}$ V560R

mAU
280 nm

Mw, kDa

Monomer
56.5 kDa

54
kDa

Elution volume, mL

B

γA4$_{3-6}$

γA4$_{3-6}$
K558R

γC3$_{3-6}$

responses normalized for mw

time (s)
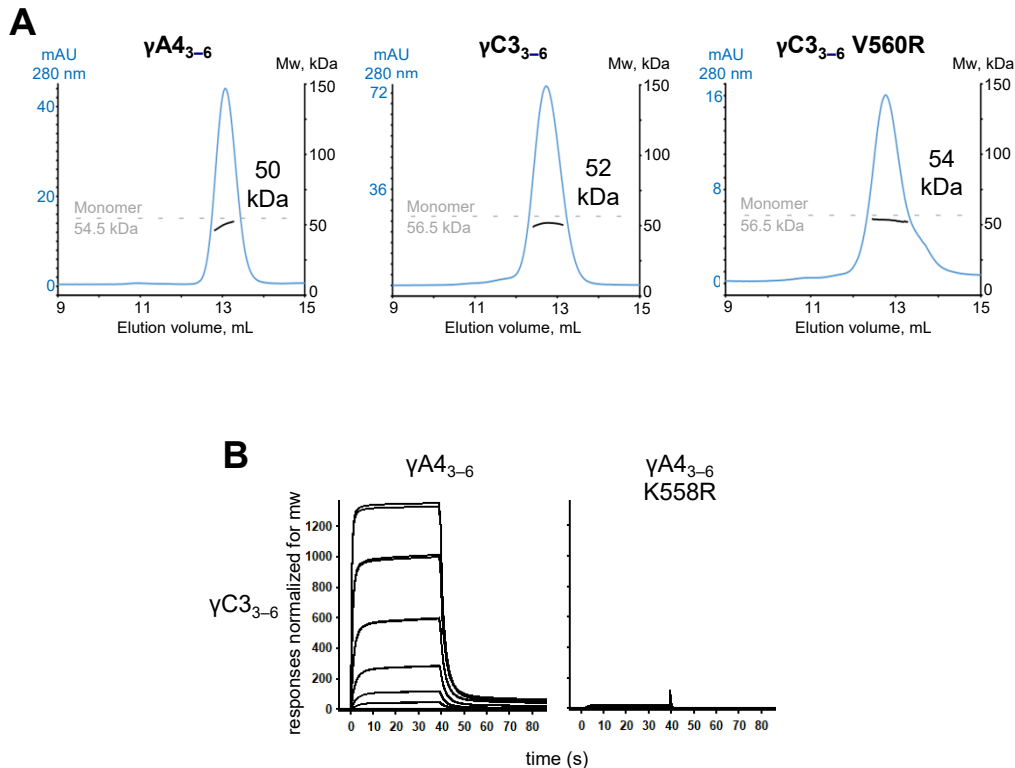
Figure 5—figure supplement 2: γA4 and γC3 *cis*-fragments behave as monomers in SEC-MALS and mutating γA4 to make it more like γC3 prevents γA4/γC3 *cis*-heterodimerization
(**A**) SEC-MALS data for wild-type γA4$_{3-6}$, wild-type γC3$_{3-6}$, and γC3$_{3-6}$ V560R showing all three molecules are monomeric in SEC-MALS, consistent with their behavior in sedimentation equilibrium AUC. Plots show size exclusion absorbance at 280 nm trace in blue (left axis), molecular weight of the eluant peak in black (right axis), and the monomer molecular weight of γA4$_{3-6}$ or γC3$_{3-6}$ measured by mass spectrometry – 54.5 kDa and 56.5 kDa respectively – as dashed grey lines. Average molecular weight of the molecules in the eluant peaks are labeled.
(**B**) SPR binding profiles for γA4$_{3-6}$ wild type and γA4$_{3-6}$ with γC3-like *cis* interface mutation K558R flowed over immobilized wild-type γC3$_{3-6}$. Loss of γC3$_{3-6}$ interaction in the presence of the K558R mutation is consistent with the SEC-MALS results shown in Figure 5.

Key Resources Table

Reagent type (species) or resource	Designation	Source or reference	Identifiers	Additional information
strain, strain background (*E.Coli*)	One shot Top10 Competent Cells	Invitrogen	C4040-06	Plasmid production
cell line (*Homo Sapiens*)	FreeStyle™ 293-F cells	Thermo Fisher Scientific	R79007	Cell line for protein expression
cell line (*Homo Sapiens*)	K-562 bone marrow chronic myelogenous leukemia (CML) cells	ATCC	ATCC CCL-243	Cell line for cell - aggregation assays
transfected construct (*M. musculus*)	$\alpha 4_{1-5}$	this paper		Pcdhα4 EC1-5, Honig/Shapiro labs
transfected construct (*M. musculus*)	$\alpha 7_{1-5}$	Rubinstein et al., 2015		
transfected construct (*M. musculus*)	$\alpha 12_{1-5}$	this paper		Pcdhα12 EC1-5, Honig/Shapiro labs
transfected construct (*M. musculus*)	$\beta 6_{1-4}$	Goodman et al., 2016a		
transfected construct (*M. musculus*)	$\beta 8_{1-4}$	Goodman et al., 2016a		
transfected construct (*M. musculus*)	$\gamma A1_{1-4}$	Goodman et al., 2016b		
transfected construct (*M. musculus*)	$\gamma A4_{1-4}$	Goodman et al., 2016b		
transfected construct (*M. musculus*)	$\gamma A8_{1-4}$	Rubinstein et al., 2015		
transfected construct (*M. musculus*)	$\gamma A9_{1-5}$	Goodman et al., 2016b		
transfected construct (*M. musculus*)	$\gamma B2_{1-5}$	Goodman et al., 2016b		

transfected construct (*M. musculus*)	$\gamma B4_{1-5}$	this paper		PcdhγB4 EC1-5, Honig/Shapiro labs
transfected construct (*M. musculus*)	$\gamma B5_{1-4}$	Goodman et al., 2016b		
transfected construct (*M. musculus*)	$\alpha C2_{1-4}$	Rubinstein et al., 2015		
transfected construct (*M. musculus*)	$\gamma C3_{1-4}$	Goodman et al., 2016b		
transfected construct (*M. musculus*)	$\gamma C4_{1-4}$	this paper		PcdhγC4 EC1-4, Honig/Shapiro labs
transfected construct (*M. musculus*)	$\gamma C5_{1-5}$	Rubinstein et al., 2015		
transfected construct (*M. musculus*)	$\alpha 7_{1-5}$-AVI	this paper		Biotinylated Pcdhα7 EC1-5, Honig/Shapiro labs
transfected construct (*M. musculus*)	$\beta 6_{1-4}$-AVI	this paper		Biotinylated Pcdhβ6 EC1-4, Honig/Shapiro labs
transfected construct (*M. musculus*)	$\beta 8_{1-4}$-AVI	this paper		Biotinylated Pcdhβ8 EC1-4, Honig/Shapiro labs
transfected construct (*M. musculus*)	$\gamma A8_{1-4}$-AVI	this paper		Biotinylated PcdhγA8 EC1-4, Honig/Shapiro labs
transfected construct (*M. musculus*)	$\gamma A9_{1-5}$-AVI	this paper		Biotinylated PcdhγA9 EC1-5, Honig/Shapiro labs
transfected construct (*M. musculus*)	$\gamma B2_{1-5}$-AVI	this paper		Biotinylated PcdhγB2 EC1-5, Honig/Shapiro labs
transfected construct (*M. musculus*)	$\alpha C2_{1-4}$-AVI	this paper		Biotinylated PcdhαC2 EC1-4, Honig/Shapiro labs
transfected construct (*M. musculus*)	$\gamma C3_{1-4}$-AVI	this paper		Biotinylated PcdhγC3 EC1-4, Honig/Shapiro labs
transfected construct (*M. musculus*)	$\gamma C4_{1-4}$-AVI	this paper		Biotinylated PcdhγC4 EC1-4, Honig/Shapiro labs

transfected construct (*M. musculus*)	$\gamma C5_{1-5}$-AVI	this paper		Biotinylated PcdhγC5 EC1-5, Honig/Shapiro labs
transfected construct (*M. musculus*)	$\alpha 4_{1-4}$-AVI	this paper		Biotinylated Pcdhα4 EC1-4, Honig/Shapiro labs
transfected construct (*M. musculus*)	$\alpha 7_{1-5}$ L301R	this paper		Pcdhα7 EC1-5 mutant, Honig/Shapiro labs
transfected construct (*M. musculus*)	$\gamma A8_{1-4}$ I116R*	Rubinstein et al., 2015		PcdhγA8 EC1-4 mutant, Honig/Shapiro labs
transfected construct (*M. musculus*)	$\beta 6_{1-4}$ R41N	this paper		Pcdhβ6 EC1-4 mutant, Honig/Shapiro labs
transfected construct (*M. musculus*)	$\gamma C5_{1-5}$ S116R	this paper		PcdhγC5 EC1-5 mutant, Honig/Shapiro labs
transfected construct (*M. musculus*)	$\beta 6_{1-4}$ S117I	this paper		Pcdhβ6 EC1-4 mutant, Honig/Shapiro labs
transfected construct (*M. musculus*)	$\beta 6_{1-4}$ L125P	this paper		Pcdhβ6 EC1-4 mutant, Honig/Shapiro labs
transfected construct (*M. musculus*)	$\beta 6_{1-4}$ E369K	this paper		Pcdhβ6 EC1-4 mutant, Honig/Shapiro labs
transfected construct (*M. musculus*)	$\beta 6_{1-4}$ Y371F	this paper		Pcdhβ6 EC1-4 mutant, Honig/Shapiro labs
transfected construct (*M. musculus*)	$\beta 6_{1-4}$ R41N/S117I	this paper		Pcdhβ6 EC1-4 mutant, Honig/Shapiro labs
transfected construct (*M. musculus*)	$\beta 6_{1-4}$ R41N/E369K	this paper		Pcdhβ6 EC1-4 mutant, Honig/Shapiro labs
transfected construct (*M. musculus*)	$\beta 6_{1-4}$ S117I/L125P	this paper		Pcdhβ6 EC1-4 mutant, Honig/Shapiro labs
transfected construct (*M. musculus*)	$\beta 6_{1-4}$ R41N/S117I/L125P	this paper		Pcdhβ6 EC1-4 mutant, Honig/Shapiro labs
transfected construct (*M. musculus*)	$\beta 6_{1-4}$ R41N/S117I/E369K	this paper		Pcdhβ6 EC1-4 mutant, Honig/Shapiro labs

transfected construct (*M. musculus*)	$\beta6_{1-4}$ R41N/S117I/Y371F	this paper		Pcdhβ6 EC1-4 mutant, Honig/Shapiro labs
transfected construct (*M. musculus*)	$\beta6_{1-4}$ R41N/S117I/L125P/E369K/Y371F	this paper		Pcdhβ6 EC1-4 mutant, Honig/Shapiro labs
transfected construct (*M. musculus*)	$\gamma C4_{1-4}$ E78A	this paper		PcdhγC4 EC1-4 mutant, Honig/Shapiro labs
transfected construct (*M. musculus*)	$\gamma C4_{1-4}$ E78Q	this paper		PcdhγC4 EC1-4 mutant, Honig/Shapiro labs
transfected construct (*M. musculus*)	$\gamma C4_{1-4}$ S344R	this paper		PcdhγC4 EC1-4 mutant, Honig/Shapiro labs
transfected construct (*M. musculus*)	$\gamma C4_{1-4}$ D290A	this paper		PcdhγC4 EC1-4 mutant, Honig/Shapiro labs
transfected construct (*M. musculus*)	$\gamma C4_{1-4}$ D290N	this paper		PcdhγC4 EC1-4 mutant, Honig/Shapiro labs
transfected construct (*M. musculus*)	$\beta1_{3-6}$	this paper		Pcdhβ1 EC3-6, Honig/Shapiro labs
transfected construct (*M. musculus*)	$\beta6_{1-6}$	this paper		Pcdhβ6 EC1-6, Honig/Shapiro labs
transfected construct (*M. musculus*)	$\beta9_{3-6}$	this paper		Pcdhβ9 EC3-6, Honig/Shapiro labs
transfected construct (*M. musculus*)	$\gamma A3_{3-6}$	this paper		PcdhγA3 EC3-6, Honig/Shapiro labs
transfected construct (*M. musculus*)	$\gamma A4_{3-6}$	Goodman et al., 2016b		
transfected construct (*M. musculus*)	$\gamma A9_{3-6}$	this paper		PcdhγA9 EC3-6, Honig/Shapiro labs
transfected construct (*M. musculus*)	$\gamma B2_{3-6}$	Goodman et al., 2016b		
transfected construct (*M. musculus*)	$\gamma B5_{3-6}$	Goodman et al., 2016b		

transfected construct (*M. musculus*)	γB7₃₋₆	Goodman et al., 2016b		
transfected construct (*M. musculus*)	αC2₂₋₆	Goodman et al., 2016b		
transfected construct (*M. musculus*)	α7₁₋₅/γC3₆ chimera	Goodman et al., 2016b		
transfected construct (*M. musculus*)	γC3₃₋₆	Goodman et al., 2016b		
transfected construct (*M. musculus*)	γC5₂₋₆	this paper		PcdhγC5 EC2-6, Honig/Shapiro labs
transfected construct (*M. musculus*)	β9₃₋₆-AVI	this paper		Biotinylated Pcdh β9 EC3-6, Honig/Shapiro labs
transfected construct (*M. musculus*)	γA4₃₋₆-AVI	this paper		Biotinylated Pcdh γA4 EC3-6, Honig/Shapiro labs
transfected construct (*M. musculus*)	γA9₃₋₆-AVI	this paper		Biotinylated Pcdh γA9 EC3-6, Honig/Shapiro labs
transfected construct (*M. musculus*)	γB2₃₋₆-AVI	this paper		Biotinylated Pcdh γB2 EC3-6, Honig/Shapiro labs
transfected construct (*M. musculus*)	αC2₃₋₆-AVI	this paper		Biotinylated Pcdh αC2 EC3-6, Honig/Shapiro labs
transfected construct (*M. musculus*)	γC3₃₋₆-AVI	this paper		Biotinylated Pcdh γC3 EC3-6, Honig/Shapiro labs
transfected construct (*M. musculus*)	γC5₂₋₆-AVI	this paper		Biotinylated Pcdh γC5 EC2-6, Honig/Shapiro labs
transfected construct (*M. musculus*)	γA4₃₋₆ V560R	this paper		PcdhγA4 EC3-6 mutant, Honig/Shapiro labs
transfected construct (*M. musculus*)	γC3₃₋₆ V560R	this paper		PcdhγC3 EC3-6 mutant, Honig/Shapiro labs
transfected construct (*M. musculus*)	γA4₃₋₆ K558R	this paper		PcdhγA4 EC3-6 mutant, Honig/Shapiro labs

transfected construct (*M. musculus*)	γC3$_{3-6}$ R558K	this paper		PcdhγC3 EC3-6 mutant, Honig/Shapiro labs
transfected construct (*M. musculus*)	γB7$_{3-6}$ Y532G	Goodman et al., 2017		
transfected construct (*M. musculus*)	γB7$_{3-6}$ A570R	this paper		PcdhγB7 EC3-6 mutant, Honig/Shapiro labs
peptide, recombinant protein	NeutrAvidin-HRP	Thermo Fisher Scientific	31030	Biotinylated protein western bot
peptide, recombinant protein	NeutrAvidin protein	Thermo Fisher Scientific	31000	SPR assays
peptide, recombinant protein	BSA	Sigma Aldrich	A7906	SPR assays
commercial assay or kit	Spin Miniprep Kit	Qiagen	27106	
commercial assay or kit	Hi-speed Plasmid Maxi Kit	Qiagen	12663	
commercial assay or kit	SF Cell Line 4D-Nucleofector® X Kit S	Lonza	V4XC-2032	
commercial assay or kit	Amine-coupling kit	Cytiva	BR100050	SPR experiments
commercial assay or kit	Morpheus Amino Acids	Molecular Dimensions	MD2-100-77	Crystallography
commercial assay or kit	Morpheus Buffer System II	Molecular Dimensions	MD2-100-101	Crystallography
chemical compound	Polyethylenimine	Polysciences	24765-2	transfection
chemical compound	Biotin	Sigma Aldrich	B4501	protein biotinylation
chemical compound	Tris Base	Fisher Scientific	BP152-5	
chemical compound	Sodium Chloride	Fisher Scientific	S271-10	
chemical compound	Calcium Chloride Dihydrate	JT Baker	1336-01	

chemical compound	Imidazole	ACROS	301870025	
chemical compound	HEPES	Sigma Aldrich	H3375	
chemical compound	Tween-20	Sigma Aldrich	P7949	
chemical compound	Sodium Acetate	Sigma Aldrich	S7545	
chemical compound	IMAC Sepharose 6 Fast Flow	Cytiva	17092109	
chemical compound	Penicillin Streptomycin	Thermo Fisher Scientific	15070063	
chemical compound	PEG 6,000	Sigma Aldrich	81260	
chemical compound	PEG 8,000	Sigma Aldrich	89510	
chemical compound	Ethylene Glycol	Fluka	03760	
chemical compound	Lithium Chloride	Sigma Aldrich	L8895	
chemical compound	MES	Sigma Aldrich	M3671	
chemical compound	Glycerol	ACROS	332031000	
software, algorithm	UCLA Diffraction Anisotropy Server	Strong et al., 2006		https://srv.mbi.ucla.edu/Anisoscal/
software, algorithm	SednTerp	Thomas Laue		http://bitcwiki.sr.unh.edu/index.php/Main_Page
software, algorithm	HeteroAnalysis	Cole et al., 2008		https://core.uconn.edu/auf
software, algorithm	Scrubber 2.0	BioLogic Software		http://www.biologic.com.au
software, algorithm	Phaser	McCoy et al., 2007		Implemented in CCP4 or Phenix (see below)
software, algorithm	CCP4	Winn et al., 2011		https://www.ccp4.ac.uk/
software, algorithm	Phenix	Liebschner et al., 2019		http://www.hkl-xray.com/

Type	Name	Source	Identifier	Notes
software, algorithm	XDS	Kabsch, 2010		http://xds.mpimf-heidelberg.mpg.de
software, algorithm	AIMLESS	Evans and Murshudov, 2013		http://www.ccp4.ac.uk
software, algorithm	Coot	Emsley et al, 2010		https://www2.mrc-lmb.cam.ac.uk/personal/pemsley/coot/
software, algorithm	PISA	Krissinel and Henrick, 2007		http://www.ebi.ac.uk/pdbe/protint/pistart.html
software, algorithm	Pymol	Schrödinger		https://pymol.org
software, algorithm	UCSF Chimera	Pettersen et al, 2004		https://www.cgl.ucsf.edu/chimera/
software, algorithm	Clustal Omega	Sievers et al., 2011		https://www.ebi.ac.uk/Tools/msa/clustalo/
software, algorithm	WebLogo 3.0	Crooks et al 2004		http://weblogo.threeplusone.com/
software, algorithm	SignalP 4.0	Peterson et al, 2011		https://services.healthtech.dtu.dk/service.php?SignalP-5.0
software, algorithm	ASTRA	Wyatt		https://www.wyatt.com/products/software/astra.html
other	Freestyle™ 23 Expression Media	Thermo Fisher Scientific	12338-018	protein expression media
other	Opti-MEM™ Reduced Serum Media	Thermo Fisher Scientific	31985-070	protein expression media
other	Series S CM4 chip	Cytiva	BR100539	Biacore assays
other	Fetal Bovine Serum	Thermo Fisher Scientific	16141079	cell-aggregation assays media
other	DMEM with GlutaMAX	Thermo Fisher Scientific	10569010	cell-aggregation assays media